Cavity-Enhanced Direct Frequency Comb Spectroscopy: Technology and Applications

Florian Adler, Michael J. Thorpe, Kevin C. Cossel, and Jun Ye

JILA, National Institute of Standards and Technology, and Department of Physics, University of Colorado, Boulder, Colorado 80309-0440;
email: fadler@jila.colorado.edu, ye@jila.colorado.edu

Annu. Rev. Anal. Chem. 2010. 3:175–205

First published online as a Review in Advance on March 1, 2010

The *Annual Review of Analytical Chemistry* is online at anchem.annualreviews.org

This article's doi:
10.1146/annurev-anchem-060908-155248

1936-1327/10/0719-0175$20.00

Key Words

femtosecond enhancement cavity, trace-gas detection, cold-molecule spectroscopy, ultrasensitive spectroscopy, frequency-domain ultrafast spectroscopy

Abstract

Cavity-enhanced direct frequency comb spectroscopy combines broad bandwidth, high spectral resolution, and ultrahigh detection sensitivity in one experimental platform based on an optical frequency comb efficiently coupled to a high-finesse cavity. The effective interaction length between light and matter is increased by the cavity, massively enhancing the sensitivity for measurement of optical losses. Individual comb components act as independent detection channels across a broad spectral window, providing rapid parallel processing. In this review we discuss the principles, the technology, and the first applications that demonstrate the enormous potential of this spectroscopic method. In particular, we describe various frequency comb sources, techniques for efficient coupling between comb and cavity, and detection schemes that utilize the technique's high-resolution, wide-bandwidth, and fast data-acquisition capabilities. We discuss a range of applications, including breath analysis for medical diagnosis, trace-impurity detection in specialty gases, and characterization of a supersonic jet of cold molecules.

1. INTRODUCTION

Cavity ring-down detection (CRDS): measurement scheme that determines the lifetime of the light inside the cavity, which corresponds to the overall loss inside the cavity

Frequency comb: frequency-domain representation of a mode-locked laser pulse train, which shows a rigorously evenly spaced spectrum of single frequencies

CE-DFCS: cavity-enhanced direct frequency comb spectroscopy

Optical spectroscopy has long been the backbone of many applications in physics, chemistry, biology, and environmental sciences. Absorption spectra of atoms and molecules contain not only structural information but also knowledge about dynamics. Thus, they enable unique identifications of molecular species; that is, they are capable of molecular fingerprinting. Furthermore, optical spectra recovered with sufficient spectral resolution and bandwidth offer systematic and detailed information: The distribution of lines in a rotational-vibrational molecular spectrum and the individual line shapes and positions allow one to extract thermodynamic and kinetic properties, as well as an understanding of the influence of external electromagnetic fields.

Because of these utilities, vibrational spectroscopy has been very successfully employed for detecting certain molecules. A wide variety of optical and semioptical detection methods have been developed over the past few decades, and contemporary applications are numerous. For example, the challenges of modern terrorism provide an enormous potential for so-called threat-detection systems. Cavity ring-down spectroscopy (CRDS) and photoacoustic spectroscopy have been used to detect explosives or chemical warfare agents (1–4). Environmental monitoring is another important emerging application driven by pollution control and global warming. Pollutants such as ozone, carbon monoxide, formaldehyde, and nitric oxide, as well as greenhouse gases such as carbon dioxide and methane, are already monitored through the use of continuous-wave (cw) laser absorption spectroscopy, differential optical absorption spectroscopy, CRDS, and Fourier transform infrared spectroscopy (FTIR) (5–10). Trace levels of impurities contained in gases used for industrial processes can also be detected with high sensitivity via CRDS. This detection capability is very important for semiconductor manufacturing (11, 12) because the purity of the gas is directly related to the quality of the end products (e.g., semiconductor laser diodes or integrated circuits). Even medical science has found important applications for optical spectroscopy in diagnostics. Traces of a single molecular species in breath have been used to detect diseases such as asthma without the need for invasive and elaborate laboratory testing of blood samples. Identification and detection of various molecular biomarkers in breath for lung diseases, diabetes, and certain types of cancer are the subject of active research employing cw laser absorption spectroscopy (13–16).

The variety of experimental techniques used in different applications demonstrate that there is no general and ideal spectroscopic method that can satisfy the needs of all of these applications. Usually, one must find a compromise among spectral coverage, resolution, sensitivity, and data-acquisition time. The problem associated with conventional spectroscopic methods such as those mentioned above is that their performance is usually focused on only one or two particular functions. For instance, CRDS provides excellent sensitivity and resolution but sacrifices spectral bandwidth; in contrast, FTIR exhibits wide detection bandwidth, but requires long acquisition times to achieve good resolution and sensitivity. These are just two examples that illustrate the shortcomings of standard optical spectroscopic techniques. Depending on a particular application, compromises can be made; however, given the increasingly demanding scientific goals associated with modern spectroscopy experiments, there is an urgent need for an advanced method that combines a broad spectral coverage with high spectral resolution while still achieving ultrahigh detection sensitivity and a rapid data-acquisition time.

Recently, the first demonstrations of employing frequency combs as ultrabroadband high-brightness light sources to tackle highly demanding spectroscopic applications (17–21) provided encouraging results. In particular, cavity-enhanced direct frequency comb spectroscopy (CE-DFCS) emerged as a powerful new technique that provides high spectral coverage, high resolution, and high sensitivity by combining the frequency comb with several other important

elements, including an external enhancement cavity and a broadband, yet highly resolving, multichannel detection system (19, 22–24).

Our goals for this review are to outline the advantage and enormous potential of CE-DFCS for numerous scientific and commercial applications and to stimulate further developments from the scientific community in order to fully exploit this technique's capabilities. The review is organized as follows. First, we present an overview of the characteristics of frequency comb sources extending from the visible to the infrared spectral region. Second, we focus on the specific challenges of achieving efficient coupling between frequency combs and femtosecond enhancement cavities. Third, we discuss contemporary spectrographic schemes designed to exploit the rapid and massively parallel nature of the data acquisition via frequency combs. Finally, we highlight some of the first applications from different scientific fields, demonstrating the potential and future directions of CE-DFCS.

Femtosecond enhancement cavity: external (usually high-finesse) passive optical cavity containing the sample gas to enhance the sensitivity in comb spectroscopy experiments

Mode-locked (or femtosecond) laser: broadband laser emitting a regular train of ultrashort pulses via (usually passive) locking of the phase across the emission spectrum

2. FREQUENCY COMB PROPERTIES AND SOURCES

2.1. Frequency Comb Fundamentals

Mode-locked lasers were originally developed to emit extremely short pulses. By the end of the 1980s, passively mode-locked, broadband dye lasers and Ti:sapphire solid-state lasers routinely generated pulses with durations significantly below 100 fs. Ten years later, the frequency-domain structure and control of such femtosecond lasers became the focus of research, leading to the development of optical frequency combs (25–27) that have since revolutionized frequency metrology and ultrafast science. **Figure 1** illustrates a pulse train emitted by a mode-locked laser and

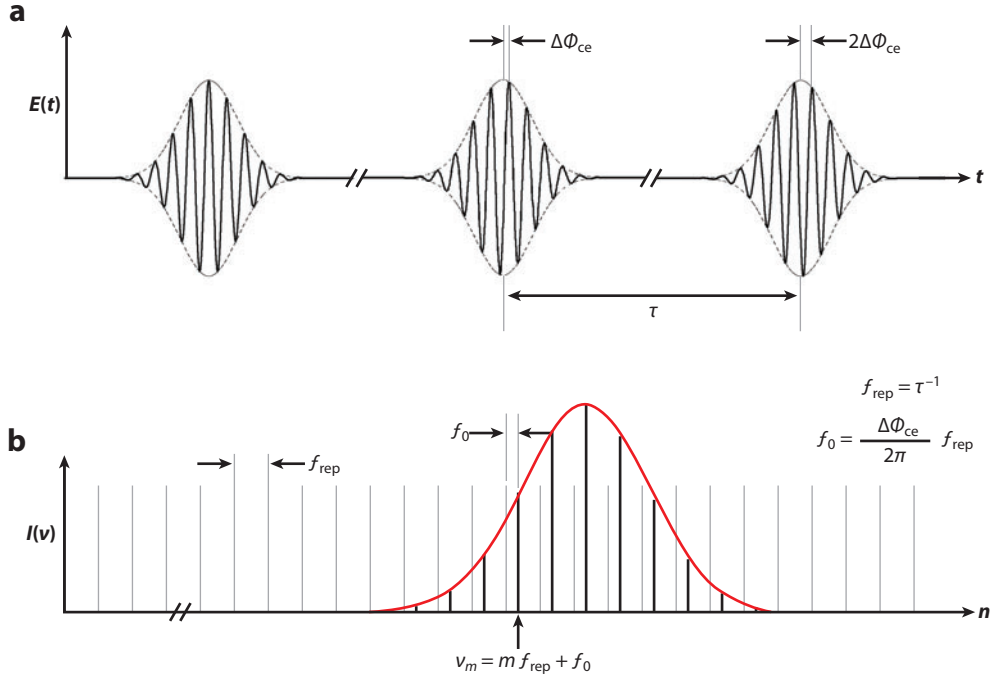

Figure 1

(*a*) Time-domain representation of a mode-locked laser pulse train and (*b*) the corresponding frequency-domain picture illustrating the frequency comb structure.

the corresponding frequency-domain picture. In the time domain, pulses with the same intensity profile exhibit a regular separation given by the laser cavity's round-trip time τ. However, due to intracavity dispersion, the pulses are not entirely identical; the electric-field oscillation (carrier) experiences a continuous pulse-to-pulse phase shift, $\Delta\phi_{ce}$, with respect to its envelope. The Fourier transform of this time series of pulses gives an expression that determines the frequency of every line m of the frequency comb by

$$\nu_m = mf_{rep} + f_0, \tag{1}$$

where f_{rep} is the laser repetition rate and f_0 is the comb offset frequency (also known as carrier-envelope offset frequency). These parameters are given by

$$f_{rep} = \frac{1}{\tau} \tag{2}$$

and

$$f_0 = \frac{\Delta\phi_{ce} \cdot f_{rep}}{2\pi}. \tag{3}$$

The repetition rate of a mode-locked laser typically ranges between 10 MHz and several gigahertz, whereas the comb offset can take on values of

$$0 \leq f_0 < f_{rep}.$$

Equation 1 shows that a frequency comb provides an ideal bridge between the optical frequencies ν_m and the radio frequency (rf) signals of f_{rep} and f_0. Furthermore, by determining both rf signals—f_{rep} directly and f_0 via nonlinear interferometry (28)—one may measure any optical frequency within the spectral range of the comb with extremely high precision. Therefore, the first application of combs was to link optical signals to the primary cesium microwave standard (29–31). Currently, combs are an essential component in the development, characterization, and mutual comparison of modern optical frequency standards (32–35).

Beyond their ability to establish a direct frequency link over vast spectral gaps, combs can also provide an unprecedented level of precision control and coherence transfer for optical fields. When properly stabilized, individual comb lines can be as narrow as the line of a cw laser, with a spacing that is extremely regular over the entire bandwidth (better than 1 part in 10^{18}) (36), and comb lines on the opposite ends of a wide spectrum show negligible phase differences (37, 38). Another outstanding feature is the fact that the spectral range can cover more than one octave from a single laser source. Therefore, frequency combs have recently found many other applications, such as high-resolution coherent control (39, 40), precision calibration of astronomical spectrographs (41, 42), precise distance measurements (43–45), direct frequency comb spectroscopy (22, 46), and production of ultracold molecules (47, 48).

The most obvious motivation to employ a comb for spectroscopy is the fact that it combines the advantages of two commonly used spectroscopic light sources: incoherent broadband continua and tunable cw lasers. The comb covers a wide spectral region, but the spectrum still consists of narrow lines, which allow for high spectral resolution when properly detected. Additionally, one may couple the comb to an optical enhancement cavity with high efficiency by matching their frequency-mode structures. Spectral brightness therefore is not compromised by the discrete transmission spectrum of the cavity. Furthermore, the fact that the frequency comb consists of femtosecond pulses in the time domain makes it relatively straightforward to employ nonlinear optics to extend its spectral coverage to regions that are not directly attainable from laser sources (e.g., the extreme ultraviolet or mid-infrared region). Consequently, comb-based

techniques such as CE-DFCS show great potential for extending current spectral coverage of traditional spectroscopy methods (49, 50).

2.2. Visible and Near-Infrared Frequency Combs

Mode-locked lasers are available throughout the visible and near-infrared spectral regions, that is, approximately from 400 nm to 2.2 μm. Over the past few decades, mode-locking has been demonstrated in various types of lasers, including dye lasers, solid-state lasers, and fiber lasers that may use exotic dopants and host materials. For real-world applications, however, the laser system needs to satisfy certain requirements such as performance, reliability, user-friendliness, and reasonable cost. For a frequency comb, stability and controllability are two important additional demands on the laser system. Therefore, nearly all experimentally employed frequency combs are based on a Ti:sapphire, Er:fiber, or Yb:fiber laser. Also, all these systems (*a*) can emit a wide spectrum with a sub-Hertz comb line width when properly controlled (51–54), (*b*) can produce pulses with high peak power capable of utilizing nonlinear optics, and (*c*) are commercially available in reasonably compact packages. **Table 1** summarizes the typical properties of such systems.

Photonic crystal fiber (PCF): nonlinear fiber generally used for supercontinuum generation; a microstructured pattern of air holes around the core (typical diameter 1.0–3.0 μm) increases the mode confinement and drastically modifies the dispersion characteristics

2.2.1. Ti:sapphire. Mode-locked Ti-doped sapphire lasers were the first systems that allowed the generation of an octave-spanning spectrum and subsequently the first self-referenced frequency combs. The Ti:sapphire crystal has a very wide gain spectrum, which allows the generation of spectra of approximately 100 THz bandwidth directly in the oscillator, corresponding to ultrashort pulses with durations of approximately 10 fs. Therefore, Ti:sapphire lasers can utilize nonlinear effects very efficiently. Spectral broadening to more than one octave is generally achieved through the use of a photonic crystal fiber (PCF) (55, 56). Octave-spanning spectra generated directly from the oscillator were also demonstrated later (57, 58). The Ti:sapphire comb covers the visible part of the spectrum with extension toward the near-infrared region (up to ~1.2 μm) and can deliver several watts of average output power. Because it is a free-space laser system, the cavity must be carefully engineered for good stability. The compactness and cost of the system are generally limited by the necessary high-power (>5-W) solid-state pump lasers—usually frequency-doubled cw Nd:YVO_4 lasers operating at 532 nm. The laser cavity itself can be built in an extremely compact framework, providing the highest repetition rate of all comb sources. Recently, a 10-GHz Ti:sapphire comb was demonstrated (59).

2.2.2. Er:fiber. Frequency combs from Er-doped fiber lasers (60–64) were originally interesting because of the widespread use of Er:fiber amplifier technology in optical communication systems (65). Therefore, Er:fiber lasers may be built from compact, inexpensive, and extremely reliable

Table 1 Typical parameters of Ti:sapphire, Yb:fiber, and Er:fiber frequency combs[a]

	Ti:Sapphire	Yb:Fiber	Er:Fiber
Wavelength range (directly)	0.7–0.9 μm	1.0–1.1 μm	1.4–1.6 μm
Wavelength range (supercontinuum)	0.4–1.2 μm	0.6–1.5 μm	1.0–2.2 μm
Maximum repetition rate	10 GHz	1 GHz	250 MHz
Output power (average)	<3 W	<75 W	<0.5 W
System design	Oscillator only	Oscillator and amplifier	Oscillator and amplifier
Octave spanning	With PCF or directly	With PCF	With HNF

[a]Abbreviations: HNF, highly nonlinear fiber; PCF, photonic crystal fiber.

industrial components such as the 980-nm grating-stabilized pump laser diodes and fiber-optic couplers, splitters, and multiplexers. The cavity of a fiber laser consists mainly of a closed beam path that makes these systems inherently stable. Their emission wavelength of approximately 1.55 μm also allows the use of highly nonlinear fibers (HNFs) for spectral broadening (66). In contrast to PCFs and related fibers with air holes, these nonlinear silica fibers consist of solid cladding and core (diameter ~4.0 μm), which allows them to be spliced onto standard communication fibers with low loss. Consequently, a higher level of integration is possible for Er:fiber systems, which improves the overall stability. Modern Er:fiber combs provide repetition rates as high as 250 MHz, average powers of several hundred milliwatts, and excellent long-term stability; they are also cost-effective, compact, and extremely user-friendly (turnkey operation).

Highly nonlinear fiber (HNF): nonlinear fiber for supercontinuum generation at wavelengths around 1.5 μm; its structure is more conventional compared to PCFs, with solid cladding and core (typical diameter ~4.0 μm)

2.2.3. Yb:fiber. Yb-doped femtosecond fiber lasers have the same basic design as Er:fiber systems and exhibit similar advantages such as turnkey operation, compactness, and high intrinsic stability. Their shorter operation wavelength of approximately 1.03 μm, however, does not allow them to employ as many industrial components and requires the use of PCFs or similar fibers for spectral broadening. Yb:fiber combs are mostly recognized for their excellent high-power capabilities. Due to the small pump defect of the laser transition (976-nm pump, 1.03-μm emission) and the availability of fibers with extremely high doping concentrations, amplified Yb:fiber systems exhibit tens of watts of output powers (53, 67). Also, demonstrated repetition rates can be as high as 1 GHz (68). Therefore, these systems seem to be the ideal choice for extending comb technology into the ultraviolet (50, 69, 70) and infrared (71) regions via nonlinear frequency conversion.

2.3. Extending Frequency Combs into the Mid-Infrared

The strongest vibrational transitions in molecules are located in the mid-infrared spectral region, between 2.5 and 12 μm (~800–4000 cm^{-1}). The sources presented in the previous section cannot cover this region directly; thus, vibrational overtones must be targeted when these frequency combs are employed. **Table 2** summarizes the line strengths of several prominent molecules as given in the HITRAN database (72) for three spectral regions (visible/near-infrared, shortwave mid-infrared, and long-wave mid-infrared). Because of the considerably stronger line intensities in the mid-infrared compared to the visible or near-infrared, the absorption signals are enhanced on average by a factor of 100 for most simple molecules, resulting in a more favorable minimum

Table 2 Room-temperature absorption line strength in 10^{-21} cm^2/(molecule cm) for simple and common molecules in different spectral regions from visible to mid-infrared[a]

	Visible/near-infrared	Shortwave mid-infrared	Long-wave mid-infrared
Wavelength	0.7–2.0 μm	2.5–5.0 μm	5.5–12 μm
Wave numbers	5,000–14,500 cm^{-1}	2,000–4,000 cm^{-1}	800–1,800 cm^{-1}
CO_2	0.3	3000	0.03
CO	0.02	300	0
CH_4	1	100	50
C_2H_2	10	200	100
H_2O	20	200	200
NH_3	5	10	200
NO	0.04	0.3	20

[a]Source: HITRAN database (72).

detectable concentration. Because mode-locked lasers in the appropriate spectral region are still in an early stage of development (73), mid-infrared frequency combs must be generated via nonlinear optical conversion starting from visible or near-infrared lasers.

DFG: difference-frequency generation

OPO: optical parametric oscillator

Fan-out periodically poled lithium niobate (PPLN): nonlinear crystal with periodic poling for quasi–phase matching with linearly varying poling period over the width of the crystal

2.3.1. Difference-frequency generation. The most direct approach for producing a mid-infrared comb is via difference-frequency generation (DFG). Mode-locked Ti:sapphire lasers provide a sufficiently wide spectrum in which to directly perform DFG (74–77); that is, a mid-infrared comb is created by mixing spectral components of the high-frequency and low-frequency wings of the original comb. Because this scheme generally uses low-intensity spectral tails and provides limited tunability of the temporal overlap, the efficiency is typically very low. Higher DFG output powers have been demonstrated by mixing two separate pulse trains that are synchronized and phase locked (78, 79), allowing the use of strong spectral features to produce highly efficient nonlinear mixing. The implementation of this scheme has been particularly successful with Er:fiber combs broadened by HNFs because the output of the nonlinear fiber generates two easily tunable and broadband spectral peaks at either side of the fundamental Er:fiber laser spectrum (80). By mixing either the shortwave part (<1.0–1.4 μm) or the long-wave part (1.6–>2.0 μm) with the strong fundamental from a parallel amplifier branch (centered at 1.55 μm) in a nonlinear crystal, milliwatt-level mid-infrared radiation has been generated between 3 and 5 μm (2000–3000 cm^{-1}) (81) and between 5 and 10 μm (1000–2000 cm^{-1}) (82), respectively. Given that different amplifiers share the same master oscillator, no active synchronization is necessary owing to the extremely low relative timing jitter (83).

2.3.2. Optical parametric oscillators. Although the power levels generated via DFG are steadily increasing, they are still too low to be used for real-world CE-DFCS experiments, which require a certain minimum power–per–comb mode on the order of 1 μW. Because they typically produce higher output power, optical parametric oscillators (OPOs) are an attractive alternative to DFG systems. Although the underlying optical parametric generation process, in which a higher-energy pump photon is converted to two lower-energy photons (signal and idler), is generally very inefficient, a resonant cavity surrounding the nonlinear crystal dramatically enhances the parametric gain, thus forming an oscillator. Through the use of this technique, frequency combs with idler powers of hundreds of milliwatts have been generated via various crystals (84–91); however, a stabilized high-power frequency comb in the spectrally important window beyond 2.5 μm (<4000 cm^{-1}) was demonstrated only recently (71).

We have developed a high-power, tunable OPO frequency comb using a fan-out periodically poled lithium niobate (PPLN) crystal that covers 2.8 to 4.8 μm. The OPO is designed to be singly resonant for the signal wavelength (1.37–1.76 μm). The cavity length is matched to the 136-MHz repetition rate of the pump laser, which is a 10-W average-power femtosecond Yb:fiber comb with a center wavelength of 1.07 μm (53, 67). Because the OPO is specifically designed to provide mid-infrared light, the setup contains only an output coupler for the idler (95% transmission). **Figure 2*a*** shows the idler output power over the OPO tuning range for a pump power of 8.47 W. The idler power exceeds 1 W over a tuning range of more than 1 μm. The measured conversion efficiency agrees well with the trend expected from the reflectivities of the cavity mirrors. The peak power of the system is 1.50 W with 9.17 W of pump power. **Figure 2*b*** depicts a collection of idler spectra over the tuning range of 2.8 to 4.8 μm (corresponding to 2080–3570 cm^{-1}); the maximum simultaneous bandwidth is approximately 280 cm^{-1}. A main feature of the system is the easy and continuous spectral tunability owing to the fan-out design of the PPLN crystal. The center wavelength is tuned by translating the crystal; changing the pump wavelength or crystal angle is not required, significantly simplifying the operation. The OPO can also run as a fully

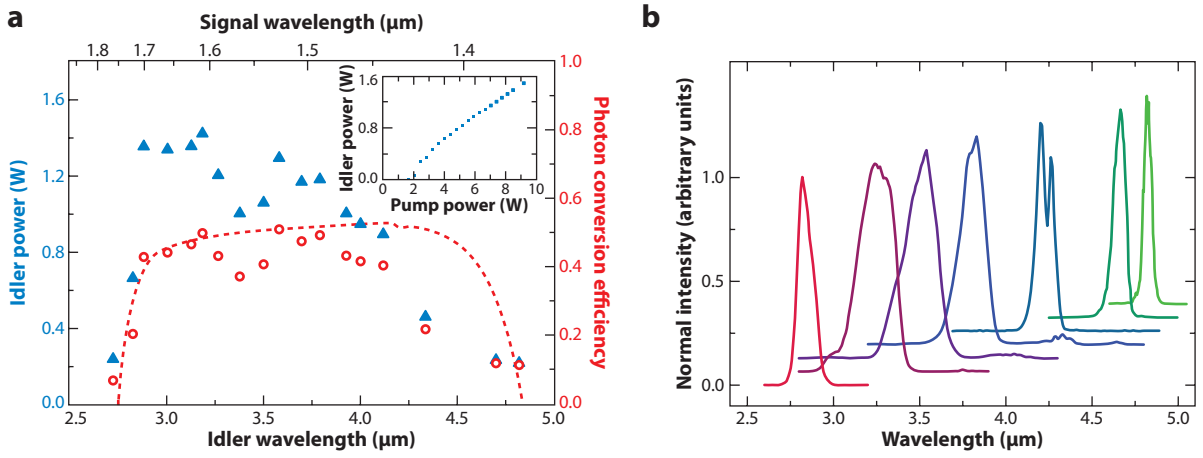

Figure 2

Characterization of the idler output from a mid-infrared optical parametric oscillator (OPO) pumped by a femtosecond Yb:fiber laser. (*a*) Idler output power (*blue triangles*) and photon-conversion efficiency (*red open circles*) for different center wavelengths. The red dashed line indicates the expected trend for the conversion efficiency calculated from the mirror reflectivities. (*Inset*) The slope efficiency curve at an idler wavelength of 3.01 μm. (*b*) Typical idler spectra throughout the OPO tuning range; the maximum simultaneous bandwidth for the idler is 0.3 μm. Reproduced from Reference 71.

stabilized comb (where f_{rep} and f_0 are locked) with an individual tooth line width of 40 kHz in the mid-infrared region (71).

3. FEMTOSECOND ENHANCEMENT CAVITIES

The Lambert-Beer law states that the transmitted intensity through a sample with the frequency-dependent absorption coefficient $\alpha(\nu)$ decreases exponentially with the length l of the sample:

$$I(l, \nu) = I_0 \exp[-\alpha(\nu) l]. \quad (4)$$

For weakly absorbing molecules, the detected relative absorption signal is approximately linear with the length of the sample. Experimentally, this length is usually limited by the size of the setup or the maximally available sample volume. Often, multipass cells—such as White or Herriott cells (92, 93)—that are formed by two opposing mirrors are used to increase the optical beam path through the sample. For further improvement in effective path lengths, the mirrors can also be aligned to form a passive Fabry-Pérot cavity, which is used in CRDS and other cavity-enhanced absorption spectroscopy experiments. CE-DFCS also employs cavities with highly reflective mirrors, but the wide bandwidth of the source sets additional requirements for mirrors used in a femtosecond enhancement cavity.

3.1. Characteristics of Optical Cavities

A passive optical cavity is characterized mainly by the quality of its resonance (the finesse, $\mathcal{F}$), which directly relates to the cavity's enhancement factor. The use of a frequency comb, however, requires optimization of broadband performance, which means that additional properties such as spectral bandwidth and intracavity dispersion have to be taken into account.

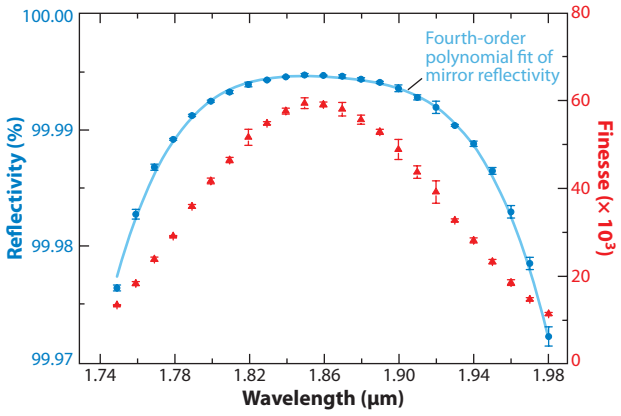

Figure 3

Mirror reflectivity (*blue circles*) and finesse (*red triangles*) for a typical near-infrared enhancement cavity measured via broadband cavity ring-down with a frequency comb; the line represents a fourth-order polynomial fit to the reflectivity data.

3.1.1. Finesse. The most important figure of merit for an optical enhancement cavity is its finesse. If there are no other losses present inside a two-mirror cavity, the finesse is directly related to the reflectivities of the two mirrors R_1 and R_2 via

$$\mathcal{F} = \frac{\pi \sqrt[4]{R_1 R_2}}{\left(1 - \sqrt{R_1 R_2}\right)}. \quad (5)$$

Our cavities generally have low loss ($\mathcal{F} > 1000$) and use two identical mirrors ($R_1 = R_2 = R$). Thus, for most practical cases Equation 5 can be simplified to

$$\mathcal{F} \approx \frac{\pi}{1 - R}. \quad (6)$$

Figure 3 shows the mirror reflectivity and finesse of a typical cavity used in near-infrared CE-DFCS. Mirror reflectivities greater than 99.9% cannot be reliably measured with standard reflectometers and are typically determined with cavity ring-down. By measuring the ring-down time τ_r, the finesse is determined via $\mathcal{F} = 2\pi\tau_r f_{\mathrm{FSR}}$, where f_{FSR} denotes the cavity free spectral range (FSR). Both single-frequency lasers and combs can be used to perform this measurement (19, 22).

The finesse determines the enhancement factor for absorption inside the cavity. In case of a differential absorption measurement, the relative change in laser intensity $\Delta I/I$ transmitted through the cavity for $\Delta I \ll I$ is given by

$$\frac{\Delta I}{I}(\nu) = \frac{\beta \mathcal{F}}{\pi} \alpha(\nu) L, \quad (7)$$

where $1 \leq \beta \leq 2$ is a factor that depends on the coupling scheme (see Section 3.2) and L is the length of the sample cell (usually equal to the length of the cavity). Compared with a single-pass measurement, the cavity enhances the absorption by $(\beta\mathcal{F})/\pi$.

3.1.2. Dispersion. For a broadband comb to be effectively coupled into the cavity, the frequency modes of the two components must be maximally matched. Whereas the comb provides evenly spaced lines (see Equation 1), the cavity FSR varies with optical frequency due to intracavity dispersion, which leads to a frequency-dependent phase shift $\phi(\omega)$, where $\omega = 2\pi\nu$; hence, the

FSR: free spectral range

longitudinal mode spacing of a linear cavity is described by

$$f_{\mathrm{FSR}}(\omega) = \frac{c}{2L + c\,\frac{\partial\phi}{\partial\omega}\Big|_{\omega_0}}, \tag{8}$$

where L is the cavity length, ω_0 is the center frequency, and c is the speed of light. The dispersion term $\frac{\partial\phi}{\partial\omega}$ causes the cavity modes to "walk off" from the comb lines with increasing distance from ω_0, limiting the bandwidth that can be coupled into the cavity simultaneously. Thus, the dispersion is an important parameter for cavities used in CE-DFCS. A dispersion measurement can be performed by determining the FSR over a wide bandwidth via single-frequency lasers or combs (22, 94–98). As discussed below, comb-cavity coupling can be optimized to minimize the impact of dispersion.

3.1.3. Spectral bandwidth. In contrast to single-frequency spectroscopic techniques with resonant enhancement, CE-DFCS requires a cavity that can provide high finesse over a wider spectral region. The dielectric mirrors that form the cavity consist of alternating quarter-wave stacks of high-index and low-index materials (e.g., TiO_2 and SiO_2). The spectral width of the high-reflectivity band is limited by the refractive index contrast between these materials. For a typical visible or near-infrared mirror, this region covers approximately 10–15% of the center wavelength. This bandwidth is significantly smaller than the spectral coverage provided by a modern frequency comb (>50% of the center wavelength), which means that the cavity is typically limiting the usable spectral range in a CE-DFCS experiment. Therefore, investigators are devoting increasing efforts to the development of alternative designs, such as a prism cavity that relies on Brewster's angle and total internal reflection to achieve a broad high-finesse region. A relative spectral bandwidth of approximately 80% with a finesse as high as 50,000 has been demonstrated in the visible and near-infrared regimes (99, 100). Such cavities, however, have increased dispersion because the beam propagates partially inside the prism. Furthermore, material absorption becomes a major concern in the infrared spectral region. Therefore, regular mirror-based cavities may be the better option. At longer wavelengths, alternate optical materials with large index differences may be used to grow mirror coatings with a relative reflectivity band that potentially exceeds 50% (101).

3.2. Cavity-Comb Coupling

Coupling a cw laser to an external cavity requires only that its frequency coincide with any cavity resonance. In contrast, a frequency comb needs to be matched in such a way that all comb lines (or as many as possible) are on resonance with corresponding cavity modes; therefore, careful mutual matching of the spacing and absolute positions of the comb and cavity modes is essential. In general, three degrees of freedom are available to adjust the coupling and lock the two together: (*a*) the frequency comb's repetition rate (f_{rep}) and (*b*) comb offset (f_0), as well as (*c*) the cavity's FSR (f_{FSR}). Their values must be preadjusted before any locking scheme can be applied. The dispersion of the cavity causes its FSR to vary with frequency; thus, comb and cavity can be matched within a limited spectral range, which decreases with increasing finesse.

3.2.1. Preadjustment procedure. As the closest match between the comb repetition rate and cavity FSR allows for the maximum number of modes to be resonant at the same time, this condition results in the highest transmission through the cavity. As shown in **Figure 4*b***, the best coupling is achieved when $f_{\mathrm{rep}} = f_{\mathrm{FSR},0}$. Here, $f_{\mathrm{FSR},0}$ denotes the cavity FSR at the spectral reference point (cavity mode n), and the comb line m matches the cavity mode n. The transmission decreases quickly as soon as the optical mode m is offset by one FSR; specifically, $f_{\mathrm{rep}} < f_{\mathrm{FSR},0}$ for

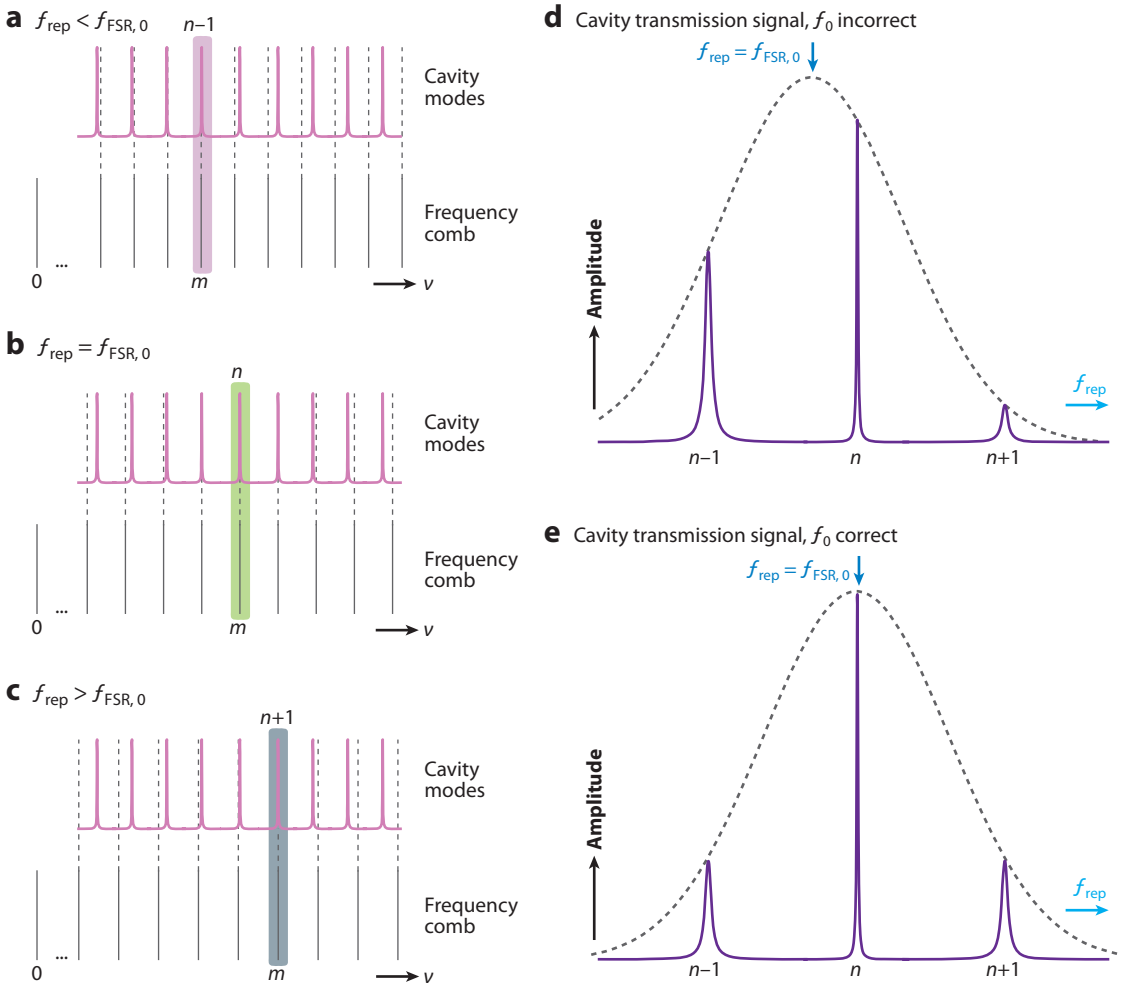

Figure 4

Schematic of a preadjustment procedure to match the comb modes to those of the cavity. (*a–c*) Adjustment of the repetition rate, f_{rep}, to match the cavity central free spectral range (FSR), $f_{FSR,0}$. (Alternatively, f_{FSR} may be varied.) The best coupling is achieved when the cavity mode n matches comb mode m, as shown in panel *b*. If the comb mode is mismatched to the cavity resonance by one FSR, coupling is not optimum, as shown in panels *a* and *c*, where $f_{rep} > f_{FSR,0}$ or $f_{rep} < f_{FSR,0}$. (*d*,*e*) Cavity transmission signal when f_{rep} is scanned. The peaks labeled $n-1$, n, and $n+1$ correspond to the situations described in panels *a*, *b*, and *c*, respectively. Panel *d* shows the incorrect choice of the comb offset f_0, and panel *e* shows the correct choice of f_0. The peak of the dashed envelope illustrates the optimum f_{rep}, which may be concealed when f_0 is off.

m matches $n-1$ or $f_{rep} > f_{FSR,0}$ for m matches $n+1$, respectively. These nonoptimum couplings are illustrated in **Figure 4*a*,*c***.

Searching for the highest transmission peak by adjusting only f_{rep} (or f_0) is not sufficient. Both parameters must be adjusted in order to find the global maximum in transmission. **Figure 4*d*** exemplifies what can happen when only f_{rep} is scanned to find the maximum coupling: If f_0 is off, the correct f_{rep} does not give the best resonant coupling, and the highest transmission peak may be falsely identified as the correct adjustment. Therefore, it is also important to look at the $n-1$ and $n+1$ transmission peaks, which exhibit different heights. When the correct f_0 is found, the

peak transmission is maximum and the side peaks have symmetric heights, clearly identifying the optimum coupling point (**Figure 4*e***). Note that any of the three involved frequencies (f_{rep}, f_0, or f_{FSR}) can be dithered to find the resonance point and that the mode spacing may be matched by adjusting f_{rep} to the cavity FSR or vice versa.

Once the initial adjustment is finished, electronic locking is implemented to maintain the optimum coupling throughout the measurement. There are two general schemes to find the best compromise among stability, efficiency, and coupled bandwidth: (*a*) tightly locking the comb to the cavity and (*b*) rapidly sweeping the comb over the cavity resonance. In the following subsections, we describe both schemes and their characteristics.

3.2.2. Locked coupling scheme. The first method relies on a tight lock between the cavity modes and the frequency comb lines. This approach assures that the comb exhibits the highest transmission through the cavity in the spectral region where the locking signal is derived; however, due to the cavity dispersion and the subsequent walk-off of the modes, this high transmission can only be maintained over a limited spectral range. **Figure 5*a*** shows schematically that, when comb line *m* is tightly locked to cavity mode *n*, there is no good match in areas farther away from the lock center. Consequently, the transmitted bandwidth is significantly decreased (typically to less than 10% of the original spectrum). To cover the entire laser spectrum, several measurements with different lock points must be made. The signal enhancement with this scheme is maximal because the light entering the cavity suppresses loss through the in-coupling mirror, resulting in $\beta = 2$ for Equation 7; however, noise usually affects the measurement because this scheme is quite sensitive to relative frequency fluctuations between the comb and the cavity. The lock itself may be achieved

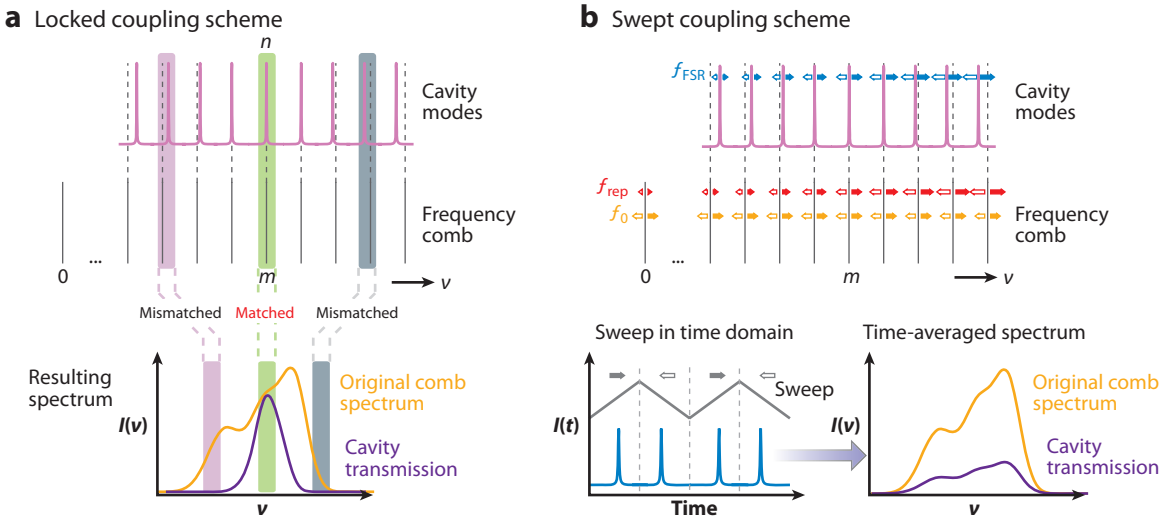

Figure 5

(*a*) A comb-cavity coupling scheme in which the comb modes and those of the enhancement cavity are locked to each other. The walk-off between cavity free spectral range (FSR) and comb f_{rep} results in the transmission spectrum (*purple*) becoming narrower than the original spectrum (*yellow*). (*b*) A coupling scheme in which pairs of comb-cavity modes are quickly swept through each other by dithering f_0 (*yellow*), f_{rep} (*red*), or f_{FSR} (*blue*). In the time domain, a single transmission peak appears for each half of the dither cycle (*blue*) under the condition that the timing resolution is coarse such that we cannot distinguish individual combs being coupled into the cavity sequentially. The resulting spectrum preserves the original bandwidth, but the average transmitted power is lower due to the sweeping duty cycle.

with different schemes, such as (*a*) locking relative positions of different spectral regions (102, 103) and (*b*) the Pound-Drever-Hall technique (96). In any case, two feedback loops are required to control, for example, the comb's f_{rep} and f_0. Note that the noise sensitivity can in principle be overcome by means of phase-sensitive detection schemes such as NICE-OHMS (noise-immune cavity-enhanced optical-heterodyne molecular spectroscopy) (104); however, application of these methods to broadband laser sources has yet to be demonstrated.

3.2.3. Swept coupling scheme. A method to overcome the negative effects of dispersion is rapid dithering of the cavity or comb modes across one another. In this scenario, all corresponding mode pairs come on resonance one after the other, which allows the full laser spectrum to be transmitted when averaging over the sweep (**Figure 5*b***). The frequency dither may be accomplished by modulating f_0, f_{rep}, or f_{FSR} with small amplitude. The two different arrow symbols indicate the breathing and/or shifting action of the comb or cavity, respectively, for alternating dither directions. **Figure 5*b*** depicts the time sequence of the transmission during fast dither cycles. Due to the cavity lifetime, all comb lines appear to be going though the cavity at the same time, resulting in a single transmission peak. To provide long-term stability, the transmission peaks are stabilized in position by a slow integrator such that the time gap between them is constant (22). This type of feedback is significantly simpler and more robust than the tight lock discussed above. However, because light is not on resonance all the time, the useful duty cycle of the experiment is compromised. As a result, the average transmission spectrum exhibits the full bandwidth of the laser source, but the power is decreased. In general, the loss in the signal strength can be overcome by sweeping fast enough to eliminate low-frequency noise, thereby preserving roughly the same signal-to-noise ratio. The resulting enhancement factor depends on the sweep speed relative to the cavity line width. For a slow dither, the situation is similar to the tight lock; hence $\beta = 2$. With an increased dither speed, the time during which the comb is on resonance becomes shorter than the intracavity photon lifetime. Consequently, the leakage suppression on the input mirror is weakened, and β approaches unity (as in CRDS). Because a faster dither speed is advantageous to overcome low-frequency noise, $\beta = 1$ is the more appropriate approximation for most experiments employing this coupling scheme.

4. HIGH-RESOLUTION SPECTROGRAPHS

Implementing frequency comb spectroscopy requires a detection system that is broadband, yet highly resolving in the spectral domain. Simple grating spectrographs can provide a resolution of several tens of gigahertz and bandwidths of hundreds of gigahertz to several terahertz; however, frequency combs typically exhibit an f_{rep} that rarely exceeds 1 GHz and bandwidths of several hundred terahertz. This means that a grating-based spectrometer falls short in both categories. Although the early-stage demonstration of CE-DFCS was performed with such a simple configuration (19), more sophisticated detection schemes are required to take full advantage of the frequency comb's characteristics.

4.1. Comb Vernier Spectrometer

The comb Vernier spectrometer contains the same basic components as a simple grating spectrograph, but it uses time as a second dimension to increase the spectral resolution. In this scheme, f_{rep} is intentionally mismatched to the cavity FSR in such a way that only every xth comb mode is on resonance, which results in an effective filtering of the original comb (**Figure 6**). This situation may be realized by choosing $f_{rep}/f_{FSR} = x/(x+1)$ or $f_{rep}/f_{FSR} = x/(x-1)$, as in a Vernier scale.

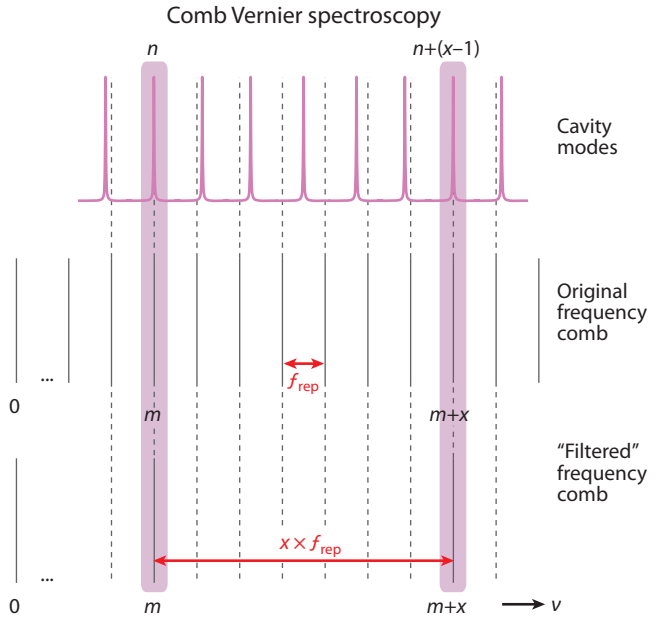

Figure 6

Schematic of a Vernier detection approach for a comb-cavity system. The repetition rate f_{rep} is intentionally mismatched to the cavity free spectral range, so that only every xth comb mode is resonant with the cavity. Consequently, the comb is filtered to contain only lines that are separated by $x \times f_{rep}$. By sweeping f_{rep}, one can tune every comb line onto resonance sequentially.

As an example, if $f_{FSR} = 100$ MHz and the spectrometer resolution is 10 GHz, a good choice would be $x = 100$. Therefore, the comb repetition rate would have to be mismatched by a factor of 100/101 ($f_{rep} = 99.0$ MHz) or 100/99 ($f_{rep} = 101.0$ MHz). This approach increases the virtual resolution of the grating spectrograph because the signal within the resolvable bandwidth originates from a single comb line. Coverage of all comb lines is then achieved by changing the lock points or slowly sweeping f_{rep}. By recording several spectra over the entire sweep, a final spectrum may be reconstructed that exhibits both a sampling period given by the comb spacing (i.e., f_{rep}) and the final spectral resolution limited by the width of an individual comb line.

Although the method can be used with the basic components of a grating spectrograph, the electronic locking and readout are more demanding. They also require more time to collect a spectrum because the mapping of spectral information into the time domain demands sequential readout. In addition, cavity dispersion and imperfect rejection of intermediate modes may be a concern. One way to simplify data collection is to use the second dimension of a two-dimensional detector array [e.g., a charge-coupled device (CCD) camera]. Here, one can use a synchronously tilting mirror to map the time dimension onto one spatial dimension of the detector array (21). In the case of a CCD camera, the mapping can also be directly obtained by clocking the camera readout.

4.2. Multiheterodyne Detection

CCD: charge-coupled device

The multiheterodyne technique employs two frequency combs with slightly different repetition rates. As combs have developed into considerably more compact and less expensive devices in recent years, this detection scheme has become more popular (105–107). In the time domain, the

offset repetition rates result in a continuously and rapidly changing time delay between pulses from the two lasers, which can be used to perform fast pump-probe spectroscopy, known as asynchronous optical sampling (108). In the frequency domain, the mismatched combs create multiple heterodyne beat notes. A comb in the rf domain is thus generated; it has a line spacing equal to the difference in f_{rep}. As an example, two 100-MHz combs are mismatched by 1 kHz, which results in an rf comb of 1-kHz spacing. The acquisition time of one full cycle is only 1 ms, which makes data collection fast. The spectral recording employs only a single-channel detector and is eventually performed with an rf spectrum analyzer or via Fourier transformation of the temporal interference trace, making it easier to resolve individual comb modes.

VIPA: virtually imaged phased array

A drawback of this scheme is that it requires two independent combs, which limits its use to primarily the visible and near-infrared regions due to the limited availability of long-wavelength combs. Mid-infrared detection has been demonstrated with a DFG source, but it suffers from the limited power available (106). If more complicated high-power systems such as OPOs (71) are used, the multiheterodyne scheme will become expensive and bulky. Furthermore, synchronization of the two combs (i.e., the stability of the mismatch frequency) has to be extremely precise because it is directly related to the attainable spectral resolution. The simultaneously recorded spectral bandwidth may also have to be reduced due to the limited dynamic range of the detector. Progress has recently been made in both synchronization quality and concurrent bandwidth, allowing the mapping of the entire laser spectrum with sufficient resolution for single comb lines (68). Furthermore, the addition of an enhancement cavity has also been demonstrated, which shows that multiheterodyne systems have potential as rapid and sensitive detection devices (109).

4.3. Virtually Imaged Phased Array Spectrometer

A completely different way to obtain high resolution is to use spectral dispersion in two spatial dimensions on a two-dimensional array. This intrinsically parallel method greatly accelerates the data-acquisition speed. This approach has been successfully implemented through use of a virtually imaged phased array (VIPA) as a component in a grating spectrograph (20). The VIPA is a special type of etalon plate that was originally designed as an alternate device for wavelength division demultiplexing (110, 111). It comprises an antireflection-coated entrance stripe that allows the light to enter the etalon. The entire surface directly above this stripe is highly reflective ($R > 99.9\%$), whereas the exit surface is coated for partial reflection ($R \sim 99.6\%$). Consequently, an interference similar to a Fabry-Pérot etalon is created; however, the VIPA is tilted at an angle (typically 1°–3°) and concurrently transmits all incident wavelengths (unlike an etalon). The VIPA provides an extremely high angular dispersion in the vertical direction (30 to 40 times better than a grating), but—just like an etalon—it generates repeating and overlapping mode orders with the FSR depending on the thickness of the plate (typically 100 GHz) (112). Therefore, a cross-dispersion grating is used in the horizontal direction to separate the VIPA orders.

Figure 7*a* shows a typical VIPA spectrometer setup, and a typical camera image of the dispersed comb is shown in **Figure 7*b***. **Figure 8** depicts the readout procedure for the image. After sample and reference images are collected, they are subtracted to produce a differential absorption image. Once the VIPA FSR is determined and a single pixel is frequency calibrated, every pixel within one FSR contains unique spectral information. The pixels are then read out column by column to retrieve a traditional one-dimensional spectrum (20, 23).

Because the VIPA spectrometer does not map any information into the time domain, it allows one to collect a relatively wide spectral region (typically 20–30 nm) coincidentally with high resolution, a feature particularly useful for experiments that study transient phenomena (24). A VIPA spectrometer can also be implemented in a compact package, which is helpful for field

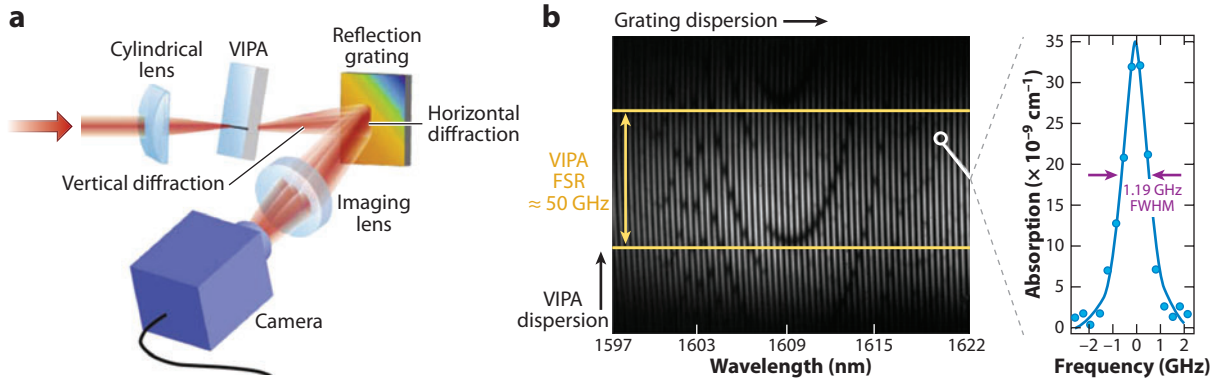

Figure 7

(*a*) Typical setup of a virtually imaged phased array (VIPA) spectrometer, consisting of a high-resolution etalon for the vertical dispersion and a coarse-resolution grating for the horizontal dispersion, which produce a two-dimensional image in which each pixel corresponds to a unique comb frequency. The incoming light is focused into the VIPA's antireflection-coated stripe with a cylindrical lens; the following cross-dispersion grating separates the VIPA orders, which are imaged onto a two-dimensional camera. (*b*) An image of a rotational spectrum of a CO_2-vibrational overtone band centered at 6215 cm^{-1} (wavelength 1609 nm) recorded with the VIPA spectrometer. The yellow bars indicate the VIPA free spectral range (FSR), and the vertical fringes are the different mode orders. The image contains 97 cm^{-1} of spectrum with a resolution of 0.027 cm^{-1} (833 MHz). The panel to the right shows the P(13) line, illustrating the excellent resolution. Abbreviation: FWHM, full width at half maximum.

deployment or in case there is limited space. A disadvantage of the VIPA system arises from the fact that it is an etalon. The fringe pattern is extremely sensitive to optical alignment; as a result, reproducibility and calibration are challenging. Furthermore, to make VIPAs work at longer wavelengths beyond the near-infrared region, one must use special infrared cameras, which are expensive and suffer from reduced sensitivity.

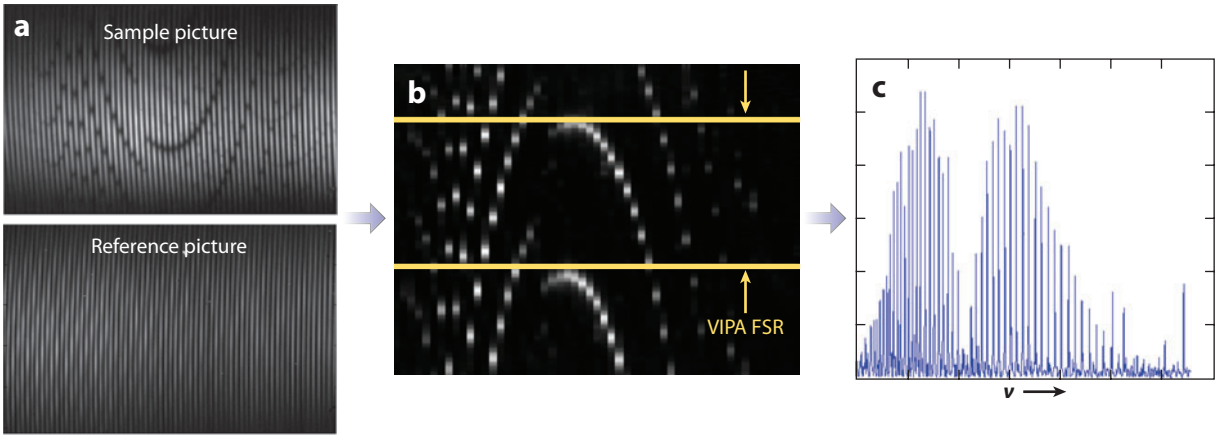

Figure 8

Generation of an absorption spectrum from virtually imaged phased array (VIPA) images. (*a*) Sample and reference images are recorded. (*b*) The nearly vertical fringes in both images are collected into column vectors and processed according to $(I_{ref} - I_{smp})/I_{ref}$ to generate the relative absorption image. After finding the etalon free spectral range (FSR; *yellow bars*) and frequency by calibrating a single pixel on the image, we can rearrange the fringes to display (*c*) the absorption spectrum in the traditional one-dimensional form.

4.4. Fourier Transform Spectrometer

Fourier transform spectroscopy (FTS) is another method through which to obtain broad bandwidth and high resolution by measuring the laser spectrum via time-domain interference (113). For example, commonly used FTIR spectrometers employ thermal light sources to cover 5–50,000 cm^{-1} with resolutions as low as 0.001 cm^{-1}. Acquisition time is a major shortcoming of FTIR spectroscopy because the resolution scales directly with the range of the scanning arm. Also, the thermal source requires a considerable averaging time to achieve a sufficiently good signal-to-noise ratio.

FC-FTS: frequency comb Fourier transform spectroscopy

Replacing the thermal source with a frequency comb—a technique known as frequency comb Fourier transform spectroscopy (FC-FTS)—immediately provides increased brightness and reduces the averaging times (114, 115). However, an even greater potential was recently unveiled (116). Because the comb is a pulsed laser source with a very precise repetition rate, an effective modulation/lock-in detection scheme that samples exactly at f_{rep} can be used. Unlike usual modulation frequencies, which are in the kilohertz range, f_{rep} is typically 100 MHz and above, which virtually eliminates any low-frequency noise. In addition to the brightness factor (a decrease of approximately tenfold in averaging time) the lock-in detection may add another factor of 10^5 in improvement (116). Although this first demonstration was performed in the near-infrared region, the scheme may be directly extended to the mid-infrared region with suitable detectors. In principle, it is also possible to combine FC-FTS with an enhancement cavity. In this case, the locked cavity-comb case would initially be better because the simpler swept-locking scheme must be modified to avoid a significant loss in duty cycle.

5. APPLICATIONS

The capabilities of CE-DFCS make it useful in a wide variety of applications. In our laboratory, we have performed CE-DFCS in the wavelength range from 0.7 to 2 μm using several different comb lasers and various nonlinear spectral broadening strategies. In this section, we elucidate four of the first spectroscopic demonstrations performed with CE-DFCS. The first three examples focus on the broadband and sensitive detection of trace levels of multiple species or different isotopes. Specifically, breath analysis involves the search for trace molecules that are believed to be biomarkers for certain diseases or body functions, and impurity detection aims to find small amounts of contaminants in specialty gases for industrial processes. The fourth example provides the first demonstration of CE-DFCS for spectroscopy of cold molecules, with an emphasis on high spectral resolution and rapid data acquisition.

The basic setup (**Figure 9**) is shared by all the experiments described in this section. The frequency comb is coupled to a high-finesse enhancement cavity via the swept coupling scheme. A VIPA spectrometer is used for detection after the cavity. The camera used for detection is either an InGaAs camera (for wavelengths below 1.7 μm) or an InSb camera (above 1.7 μm); both arrays have 320 × 256 pixels.

5.1. Trace-Gas Detection I: Breath Analysis

Breath analysis has been the subject of active research in medical diagnostics for decades (117–120). Many investigations have demonstrated that some molecules in the breath—particularly volatile organic compounds, as well as several inorganic molecules—are potential markers for certain diseases. Studies include cw laser–based detection of methane, ethane, or hydrogen peroxide as markers for inflammatory lung diseases or lung cancer (14, 15, 121), formaldehyde as an indicator

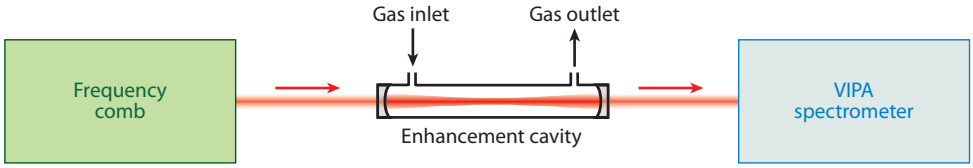

Figure 9

Basic scheme of a typical trace detection setup that uses cavity-enhanced direct frequency comb spectroscopy. The broadband frequency comb is coupled into the optical enhancement cavity that contains either the sample or a reference gas. The cavity-transmitted comb spectrum is resolved and detected by the virtually imaged phased array (VIPA) spectrometer.

for breast cancer (15), acetone as a tracer for diabetes (16), and hydrogen peroxide and nitric oxide as asthma markers (122, 123), as well as the analysis of a variety of heavier hydrocarbons with mass spectrometers in the breath of lung and breast cancer patients (124–126). However, many of these studies could not provide conclusive results.

CE-DFCS may become a valuable addition to current analytical techniques due to its superb combination of resolution, sensitivity, and detection bandwidth. The possibility of using one spectroscopic system to unambiguously identify and quantify multiple important molecular species may allow breath analysis to become a reliable and realistic diagnostic medical tool. Recently, the first such study was performed to test the potential of CE-DFCS to detect biomarkers in human breath through the use of a near-infrared Er:fiber frequency comb (23). A particular difficulty in analyzing breath samples is the high abundance of H_2O and CO_2, which may easily screen nearby absorption lines of trace molecules at the parts-per-million or parts-per-billion level. **Figure 10** shows a spectrum of human breath, at approximately 6130 cm^{-1}, that is dominated mostly by CH_4 and H_2O; however, the inset demonstrates our ability to observe weak lines (such as those of several isotopes of CO_2) in this spectral window by utilizing high spectral resolution. Future breath studies will focus on the mid-infrared region, in which one can detect most of the potential breath markers mentioned above, thereby taking advantage of the increased line strengths and the high selectivity offered by CE-DFCS.

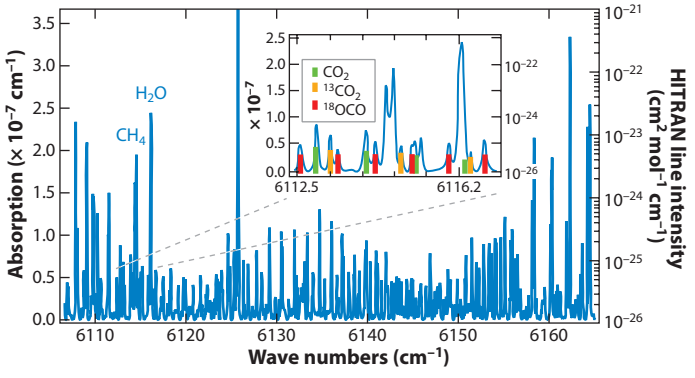

Figure 10

Cavity-enhanced direct frequency comb spectroscopy–based detection of a breath spectrum between 6105 and 6165 cm^{-1} with various lines from H_2O, CH_4, and CO_2. (*Inset*) An expanded region in which several CO_2 isotopes can be observed. Color bars indicate line positions from HITRAN (72).

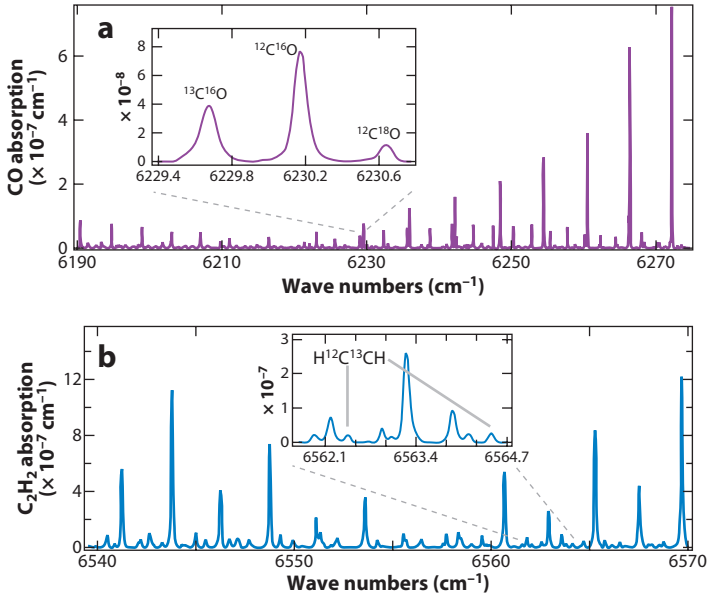

Figure 11

(*a*) The isotope spectrum of CO near 6230 cm^{-1} at a concentration of 4.5 parts per thousand. (*b*) The isotope spectrum of C_2H_2 near 6550 cm^{-1} at a concentration of 2.2 parts per million. The unlabeled lines in the C_2H_2 inset spectrum are $^{12}C_2H_2$, and the labeled lines are $H^{12}C^{13}CH$.

5.2. Determination of Isotope Ratios

The determination of isotope ratios has proved to be a powerful tool in medical analysis, geology, and climate research. Optical detection of these ratios is based on spectral shifts of transition frequencies associated with different isotopes. Intentionally ingesting substances with enriched isotope content (e.g., ^{13}C or D) allows one to track body functions by measuring the exhaled isotope ratios $^{13}CO_2/^{12}CO_2$ or HDO/H_2O over time or under certain circumstances (127, 128). Stable isotopes of H_2O, CO_2, and O_2 are analyzed in ice cores to track the history of the Earth's climate, to study atmospheric processes, and to observe groundwater transport (129–132).

Over the course of the first trace detection studies with CE-DFCS, it became apparent that the technique could also be used to determine isotope ratios. The wide spectral bandwidth allows for the detection of a variety of different species and their isotope bands, and the high spectral resolution makes it easy to separate and identify different isotope spectral lines. Furthermore, the recording of many lines from the same molecular species increases the precision of the ratio measurement. **Figure 11** shows examples of spectral features that were recovered through the use of an Er:fiber laser in the 1.6-μm-wavelength region of CO, C_2H_2, and their corresponding isotope bands.

5.3. Trace-Gas Detection II: Impurities in a Semiconductor Specialty Gas

Trace detection: refers to an experiment designed to detect particular molecules in extremely small (trace) quantities

Industrial processing gases sometimes require an extremely high level of purity. Some of the best examples are the gases used for semiconductor manufacturing, including silane (SiH_4), germane (GeH_4), phosphine (PH_3), and arsine (AsH_3). For techniques such as molecular beam epitaxy or chemical vapor deposition to perform well, the growth of semiconductor devices such as integrated circuits and laser diodes requires the use of extremely pure raw materials. Any impurities in the processing gas—even at trace-level concentrations—have a direct negative effect on the

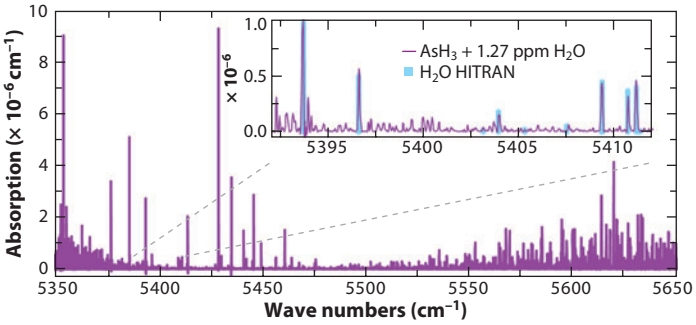

Figure 12

Spectrum of arsine gas with trace impurities of water. (*Inset*) A spectral window in which several absorption peaks associated with water at a concentration of approximately 1.27 ppm are clearly identifiable within the arsine spectrum. The H_2O reference lines indicated in blue are from the HITRAN database (72).

devices' performance and lifetime (11, 12, 133). The incorporation of contaminants often results in additional donor or acceptor atoms in the crystal, which also leads to undesired disturbances of the semiconductor's band structure. The most problematic impurities depend on the type of processing gas, but typical examples include oxygen, carbon dioxide, methane, and water vapor.

There are several general problems associated with current optical and nonoptical detection of these impurities: The concentrations of interest are usually in the parts-per-billion range and below, and the processing gas itself has strong absorption bands that can obstruct lines of other molecules. Also, one must observe multiple impurities, which currently requires completely different instruments for each contaminant. The last issue makes comb spectroscopy particularly attractive for such applications due to its wide spectral coverage and its capability to reach wavelengths inaccessible by many other sources. Our laboratory is conducting the first demonstration of CE-DFCS to detect trace-level impurities in AsH_3 gas.

The experiment has been set up in a lab at the National Institute of Standards and Technology that was able to handle the extremely toxic arsine gas. In contrast to earlier experiments, we are using an HNF after the amplified femtosecond Er:fiber laser to shift the spectrum to longer wavelengths (1.75–1.95 μm or 5130–5710 cm^{-1}), where arsine is widely unexplored but is expected to have a sufficient transparency window. The enhancement cavity (see **Figure 3**) and VIPA spectrometer have been modified accordingly to operate in the same wavelength region.

Figure 12 shows the recorded spectrum of arsine containing 1.27 ppm of water vapor. The strong arsine absorption dominates most of the spectral region. Thanks to the high bandwidth and resolution of the frequency comb, one can closely examine different spectral windows at which water lines are clearly identified. From the signal-to-noise ratio of these peaks, we can conclude that water impurity can be detected at a level of 31 ppb (defined as three standard deviations above the noise) with the present setup in a pure AsH_3 gas. In principle, several other impurities, such as methane, hydrogen sulfide, carbon dioxide, and silane, are all within the range of the comb spectrum. Unfortunately, the transparency of arsine in the previously unexplored measurement region of 5130 to 5710 cm^{-1} was merely sufficient in a narrow window containing only H_2O lines (134).

5.4. Spectroscopy of a Supersonic Jet of Cold Molecules

Supersonic molecular jets are widely used in physical chemistry to obtain cold molecules without having to perform cryogenic cooling. The rapid expansion through a small nozzle into a vacuum

chamber accelerates the bulk speed of the molecules, accompanied by an isentropic cooling of their internal degrees of freedom. However, the jet is not in thermal equilibrium; that is, the rotational, vibrational, and translational temperatures of the molecular ensemble differ from one another. Furthermore, the cooling behavior varies significantly with the background and backing pressure, the involved molecules (sample and carrier gas), and the nozzle geometry (135). Consequently, studying supersonic jet expansions and their thermodynamics presents an interesting way to verify the usefulness of CE-DFCS for future spectroscopic applications to cold and ultracold molecular samples.

CE-DFCS is very promising for these types of studies. The technique's wide spectral coverage and simultaneous high spectral resolution allow for the detection of both molecular rotational distributions and spectral line shapes, thus providing insight into both internal and external degrees of freedom. Used in combination with the VIPA spectrometer, CE-DFCS permits one to take fast snapshots of the spectrum, which in turn allows the use of pulsed nozzles. Unlike continuous beams, pulsed expansions relax the requirements for high-volume pumping capability and prevent

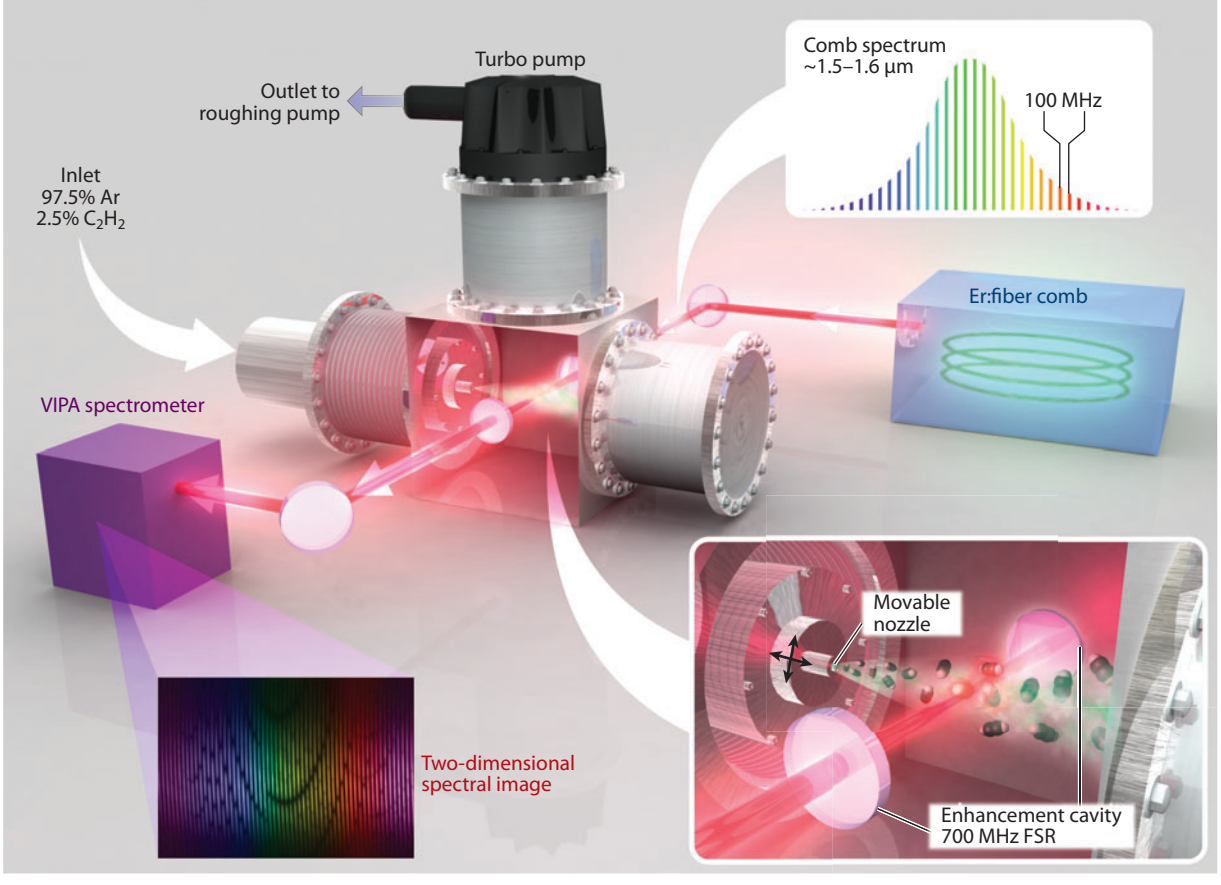

Figure 13

Schematic of the setup used to perform tomography on a supersonic expansion. The gas is released into a vacuum chamber through a movable nozzle; the absorption of the C_2H_2 molecules is probed with an Er:fiber frequency comb along the axis of the enhancement cavity. The resulting spectrum is detected with the subsequent virtually imaged phased array (VIPA) spectrometer. Abbreviation: FSR, free spectral range. Artwork by G. Kuebler, JILA.

the formation of shock waves close to the nozzle. Therefore, the use of CE-DFCS provides unprecedented advantages over previous supersonic jet investigations, which employed Raman spectroscopy, FTIR, or CRDS for the study of cooling behaviors or density distributions (136–140).

In the first demonstration of this approach, we have performed three-dimensional tomography of a supersonic expansion of acetylene in argon carrier gas (2.5% C_2H_2 and 97.5% Ar). The setup is shown in **Figure 13**. An Er:fiber frequency comb ($f_{rep} = 100$ MHz) provides full coverage of the strong $\nu_1 + \nu_3$–vibrational overtone band of C_2H_2 around 6500 cm^{-1} (1.53 μm wavelength). The jet direction (defined as the z axis) is oriented perpendicular to the enhancement cavity (the x axis), which exhibits a finesse of 6300. The comb spacing of 100 MHz, however, is too narrow to resolve the line shapes of the absorption signal (approximately 300 MHz line width). Therefore, the cavity length is set to provide an FSR that is seven times f_{rep}, which filters the comb to an effective repetition frequency of 700 MHz. This method assures that only one comb mode interacts with one molecular absorption line at a time, which results in an excellent spectral resolution of approximately 1 MHz. Then, the entire line is recorded by scanning the comb mode frequency (e.g., by scanning f_{rep}). Because the comb covers all rotational lines simultaneously, the frequency comb has to be scanned only by 700 MHz to record the full absorption band. As a frequency

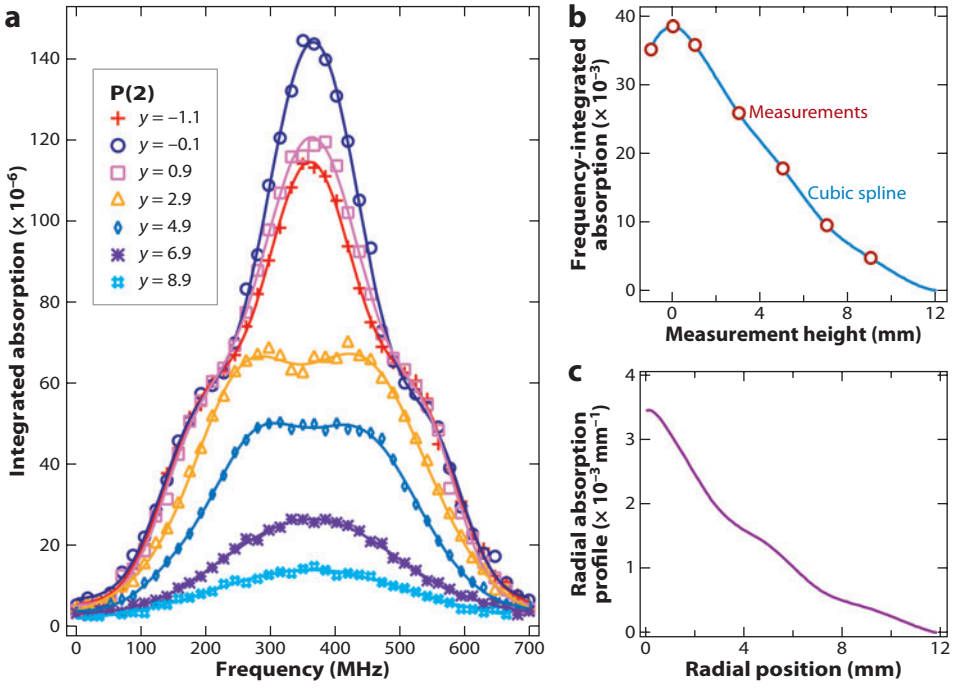

Figure 14

(*a*) Integrated absorption frequency scans (integrated along the x axis) of the P(2) transition at a distance of $z = 11$ mm from the nozzle for several heights y of the cavity mode, with respect to the axis of the expansion. The solid lines represent fits to a sum of three Gaussians, which provides an excellent fit to every absorption line shape that we observed. The triple-Gaussian line shape implies that the distribution of rotational ground states are populated differently in the center of the beam than in the surrounding region. (*b*) The data from panel *a* are frequency integrated and plotted versus y, and a cubic spline of this data is performed. (*c*) The inverse Abel transform of this cubic spline results in a radial absorption profile. Reproduced from Reference 24.

reference for the scan, the cavity is locked to a stabilized 1064-nm cw laser, which is superimposed onto the frequency comb beam.

The three-dimensional imaging is acquired with the help of a movable nozzle (circular, 1-mm diameter). The absorption line shape and rotational-state distribution are recorded for different distances from the nozzle z and height position y relative to the cavity axis. The resulting data set contains an integrated absorption along the x axis. The jet expansion features axial symmetry that allows the use of tomographic reconstruction. In this situation, the inverse Abel transform is applied, which converts the integrated projection along x into a radial profile (141, 142). **Figure 14** shows an example of the reconstruction process for the P(2) rotational line at the position $z = 11$ mm. **Figure 14*a*** displays absorption profiles obtained at different y positions; the total absorption is obtained by integrating over the frequency scan. **Figure 14*b*** plots the total absorption signal versus the height, with a cubic spline fit. The inverse Abel transform is used to obtain the radial profile as shown in **Figure 14*c***. This analysis is repeated for all rotational lines of the P and R branches. The information contained in the two branches is redundant, but analyzing both of them is an excellent consistency check for the experiment.

The resulting data from the tomography can be converted into a cross-sectional profile of the density and rotational-temperature distribution. **Figure 15** shows the density profile, with

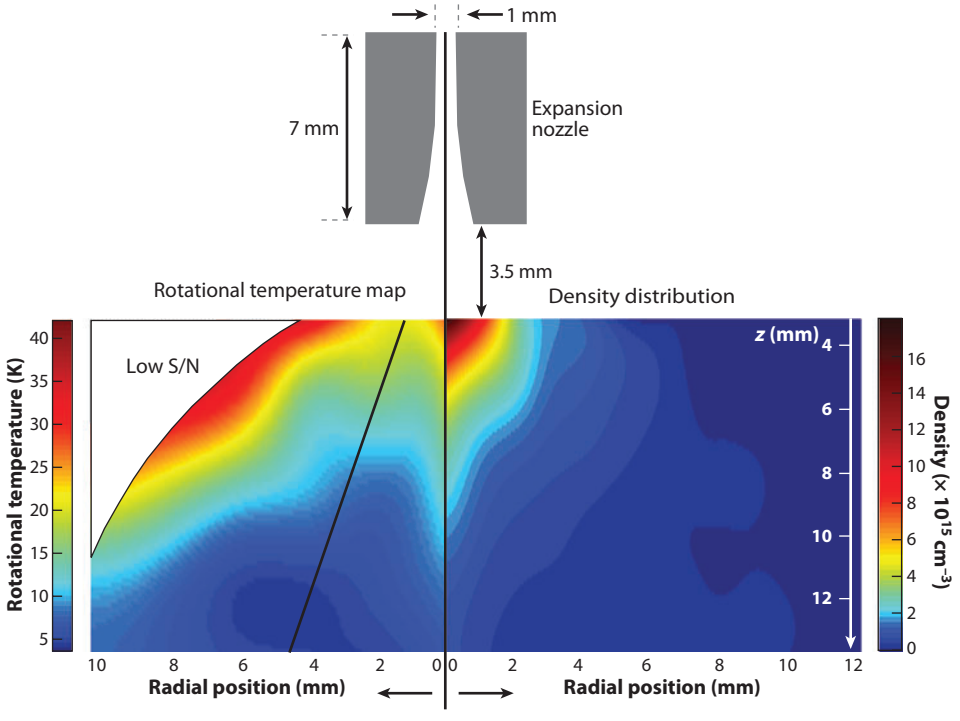

Figure 15

A scaled drawing of the supersonic expansion nozzle is shown above tomographically reconstructed two-dimensional maps of (*left*) the rotational temperature and (*right*) density. The black line in the temperature plot indicates the trajectory of molecules with a transverse velocity of 230 m s^{-1}. These molecules exhibit the fastest cooling behavior as the molecules fly away from the nozzle. Surprisingly, collisional cooling in the center of the beam is less efficient, possibly because of the Ar clustering there. Abbreviation: S/N, signal-to-noise ratio. Reproduced from Reference 24.

respect to both the radial and z positions, that exhibits the expected distribution. The anomalous cooling behavior shown in the figure is reflected in the observed unusual line shapes of the individual rotational lines, which demonstrates the usefulness of the high spectral-resolving power of CE-DFCS. A detailed analysis of this observation is provided in Reference 24; clustering of Ar atoms in the beam center, preventing efficient cooling of the C_2H_2 molecules there, may be the cause of this behavior.

6. CONCLUSION

In this review, we have highlighted CE-DFCS as a powerful method for modern molecular spectroscopy. The unique combination of broad spectral coverage, high resolution, and ultrahigh detection sensitivity makes CE-DFCS a unique enabling tool for a variety of demanding applications. In a typical experiment, more than 3000 data channels are recorded simultaneously over a bandwidth of $\sim$100 cm^{-1} with a (single-channel) detection sensitivity of less than 10^{-8} cm^{-1} $Hz^{-1/2}$. The spectral resolution can be better than 1 MHz (corresponding to 3×10^{-5} cm^{-1}) when individual comb lines are allowed to interact with a single absorption feature. Initial demonstrations with trace-gas detection and cold-molecule spectroscopy have shown this method's enormous potential and advantages. More technical development and refinement are certainly necessary to realize the full potential of CE-DFCS and to make the systems more reliable, more compact, and easier to operate. For instance, first steps have been taken to push comb spectroscopy into the mid-infrared region to allow access to strong fundamental molecular absorption bands. Given that continuous improvements lie ahead, we are positive that CE-DFCS will move decisively ahead of conventional spectroscopic techniques and will be employed more frequently in the future to contribute to exciting scientific directions and emerging fields such as spectroscopy on ultracold molecules (47, 48, 143) and controlled chemistry at low temperatures (144–146).

SUMMARY POINTS

1. CE-DFCS provides broadband, high-resolution, ultrasensitive, and rapid detection of molecular absorption in one experimental platform.
2. A low-dispersion optical enhancement cavity allows one to efficiently couple a wide-bandwidth frequency comb source into the cavity and increase the effective path length through the sample by three to four orders of magnitude.
3. Implementing high resolution, broad spectral coverage, and rapid data acquisition for frequency comb spectroscopy requires specially designed spectral detection schemes such as Vernier spectroscopy, multiheterodyne detection, VIPAs, and frequency-comb Fourier transform spectrographs.
4. Trace-gas detection experiments such as breath analysis and impurity measurements demonstrate the highly sensitive and selective nature of CE-DFCS and its capability for simultaneous detection and quantification of multiple species.
5. Tomography of a supersonic jet is an excellent example for the power of simultaneous wide bandwidth and high resolution offered by comb spectroscopy. Individual line shapes of multiple molecular absorption resonances are thereby resolved at the same time, allowing access to information regarding both external and internal degrees of freedom for molecules and drastically decreasing the acquisition time.

FUTURE ISSUES

1. To fully exploit CE-DFCS in the mid-infrared region, technology for broadband, low-dispersion, and high-finesse cavities based on mirrors or prisms needs to be advanced.
2. Efforts are currently under way to extend CE-DFCS toward the longer-wavelength mid-infrared region (in particular below 2000 cm^{-1}) by designing a new OPO based on a longer-wavelength mode-locked pump source.
3. Compact, robust, and highly reliable comb sources (preferably in the mid-infrared region) need to be developed for future commercial and portable applications.
4. More efficient pattern-recognition and database-search algorithms need to be developed to quickly identify molecular species, give better quantitative analysis, and enhance detection sensitivities.
5. To extend the scope beyond primarily proof-of-principle applications, researchers should expand both sensitivity and spectral calibration toward the fundamental limit of CE-DFCS.
6. A more comprehensive molecular transition database will need to be created to fully develop the potential of CE-DFCS for many different scientific applications.

DISCLOSURE STATEMENT

Our work is funded by the Air Force Office of Scientific Research, the Defense Advanced Research Project Agency, Agilent, the National Institute of Standards and Technology, the National Science Foundation, and the Defense Threat Reduction Agency. F.A. is supported partly by the Alexander von Humboldt Foundation. K.C.C. acknowledges graduate fellowship support from the National Science Foundation.

ACKNOWLEDGMENTS

We thank our colleagues who have made important contributions to the work presented here. In particular, A. Marian, M.C. Stowe, R.J. Jones, and K.D. Moll helped in the early development stages of CE-DFCS. D. Balslev-Clausen and M. Kirchner participated in the demonstration of breath analysis via CE-DFCS. K.A. Bertness, J. Feng, and M.W. Raynor contributed to the specialty gas impurity detection. We also thank T.R. Schibli, A. Pe'er, D.C. Yost, M.H.G. de Miranda, L. Sinclair, E.R. Cornell, S.A. Diddams, I. Hartl, M.E. Fermann, M. Zhu, D.J. Nesbitt, and D.D. Hudson for many useful discussions and technical help.

LITERATURE CITED

1. Todd MW, Provencal RA, Owano TG, Baldus BA, Kachanov A, et al. 2002. Application of mid-infrared cavity-ringdown spectroscopy to trace explosives vapor detection using a broadly tunable (6–8 μm) optical parametric oscillator. *Appl. Phys. B* 75:367–76
2. Pushkarsky MB, Dunayevskiy IG, Prasanna M, Tsekoun AG, Go R, Patel CKN. 2006. High-sensitivity detection of TNT. *Proc. Natl. Acad. Sci. USA* 103:19630–34
3. Patel CKN. 2008. Laser photoacoustic spectroscopy helps fight terrorism: high sensitivity detection of chemical warfare agent and explosives. *Eur. Phys. J. Spec. Top.* 153:1–18

4. Moore DS. 2004. Instrumentation for trace detection of high explosives. *Rev. Sci. Instrum.* 75:2499–512
5. Sigrist MW. 1994. *Air Monitoring by Spectroscopic Techniques*. New York: Wiley
6. Wang M, Zhang Y, Liu J, Liu W, Kan R, et al. 2006. Applications of a tunable diode laser absorption spectrometer in monitoring greenhouse gases. *Chin. Opt. Lett.* 4:363–65
7. Grutter M. 2002. Multi-gas analysis of ambient air using FTIR spectroscopy over Mexico City. *Atmosfera* 16:1–13
8. Brown SS. 2003. Absorption spectroscopy in high-finesse cavities for atmospheric studies. *Chem. Rev.* 103:5219–38
9. Ball SM, Jones RL. 2003. Broad-band cavity ring-down spectroscopy. *Chem. Rev.* 103:5239–62
10. Platt U, Stutz J. 2008. *Differential Optical Absorption Spectroscopy: Principles and Applications*. Berlin/Heidelberg: Springer
11. Lehman SY, Bertness KA, Hodges JT. 2003. Detection of trace water in phosphine with cavity ring-down spectroscopy. *J. Cryst. Growth* 250:262–68
12. Funke HH, Grissom BL, McGrew CE, Raynor MW. 2003. Techniques for the measurement of trace moisture in high-purity electronic specialty gases. *Rev. Sci. Instrum.* 74:3909–33
13. Dahnke H, Kleine D, Hering P, Mürtz M. 2001. Real-time monitoring of ethane in human breath using mid-infrared cavity leak-out spectroscopy. *Appl. Phys. B* 72:971–75
14. Skeldon KD, McMillan LC, Wyse CA, Monk SD, Gibson G, et al. 2006. Application of laser spectroscopy for measurement of exhaled ethane in patients with lung cancer. *Respir. Med.* 100:300–6
15. McCurdy MR, Bakhirkin Y, Wysocki G, Lewicki R, Tittel FK. 2007. Recent advances of laser-spectroscopy-based techniques for application in breath analysis. *J. Breath Res.* 1:014001
16. Wang C, Surampudi AB. 2008. An acetone breath analyzer using cavity ringdown spectroscopy: an initial test with human subjects under various situations. *Meas. Sci. Technol.* 19:105604
17. Marian A, Stowe MC, Lawall JR, Felinto D, Ye J. 2004. United time-frequency spectroscopy for dynamics and global structure. *Science* 306:2063–68
18. Gerginov V, Tanner CE, Diddams SA, Bartels A, Hollberg L. 2005. High-resolution spectroscopy with a femtosecond laser frequency comb. *Opt. Lett.* 30:1734–36
19. Thorpe MJ, Moll KD, Jones RJ, Safdi B, Ye J. 2006. Broadband cavity ringdown spectroscopy for sensitive and rapid molecular detection. *Science* 311:1595–99
20. Diddams SA, Hollberg L, Mbele V. 2007. Molecular fingerprinting with the resolved modes of a femtosecond laser frequency comb. *Nature* 445:627–30
21. Gohle C, Stein B, Schliesser A, Udem T, Hänsch TW. 2007. Frequency comb Vernier spectroscopy for broadband, high-resolution, high-sensitivity absorption and dispersion spectra. *Phys. Rev. Lett.* 99:263902
22. Thorpe MJ, Ye J. 2008. Cavity-enhanced direct frequency comb spectroscopy. *Appl. Phys. B* 91:397–414
23. Thorpe MJ, Balslev-Clausen D, Kirchner M, Ye J. 2008. Cavity-enhanced optical frequency comb spectroscopy: application to human breath analysis. *Opt. Express* 16:2387–97
24. Thorpe MJ, Adler F, Cossel KC, de Miranda MHG, Ye J. 2009. Tomography of a supersonically cooled molecular jet using cavity-enhanced direct frequency comb spectroscopy. *Chem. Phys. Lett.* 468:1–8
25. Udem T, Holzwarth R, Hänsch TW. 2002. Optical frequency metrology. *Nature* 416:233–37
26. Cundiff ST, Ye J. 2003. Colloquium: femtosecond optical frequency combs. *Rev. Mod. Phys.* 75:325–42
27. Ye J, Cundiff ST, eds. 2004. *Femtosecond Optical Frequency Comb Technology: Principle, Operation and Application*. New York: Springer
28. Telle HR, Steinmeyer G, Dunlop AE, Stenger J, Sutter DH, Keller U. 1999. Carrier-envelope offset phase control: a novel concept for absolute optical frequency measurement and ultrashort pulse generation. *Appl. Phys. B* 69:327–32
29. Jones DJ, Diddams SA, Ranka JK, Stentz A, Windeler RS, et al. 2000. Carrier-envelope phase control of femtosecond mode-locked lasers and direct optical frequency synthesis. *Science* 288:635–39
30. Diddams SA, Jones DJ, Ye J, Cundiff ST, Hall JL, et al. 2000. Direct link between microwave and optical frequencies with a 300 THz femtosecond laser comb. *Phys. Rev. Lett.* 84:5102–5
31. Holzwarth R, Udem T, Hänsch TW, Knight JC, Wadsworth WJ, Russel PStJ. 2000. Optical frequency synthesizer for precision spectroscopy. *Phys. Rev. Lett.* 85:2264–67
32. Ludlow AD, Zelevinsky T, Campbell GK, Blatt S, Boyd MM, et al. 2008. Sr lattice clock at 1×10^{-16} fractional uncertainty by remote optical evaluation with a Ca clock. *Science* 319:1805–8

33. Rosenband T, Hume DB, Schmidt PO, Chou CW, Brusch A, et al. 2008. Frequency ratio of Al^+ and Hg^+ single-ion optical clocks: metrology at the 17th decimal place. *Science* 319:1808–12
34. Lemonde P. 2009. Optical lattice clocks. *Eur. Phys. J. Spec. Top.* 172:81–96
35. Margolis HS. 2009. Trapped ion optical clocks. *Eur. Phys. J. Spec. Top.* 172:97–107
36. Ma L-S, Bi Z, Bartels A, Robertsson L, Zucco M, et al. 2004. Optical frequency synthesis and comparison with uncertainty at the 10^{-19} level. *Science* 303:1843–45
37. Ye J, Hall JL, Diddams SA. 2000. Precision phase control of an ultrawide-bandwidth femtosecond laser: a network of ultrastable frequency marks across the visible spectrum. *Opt. Lett.* 25:1675–77
38. Martin MJ, Foreman SM, Schibli TR, Ye J. 2009. Testing ultrafast mode-locking at microhertz relative optical linewidth. *Opt. Express* 17:558–68
39. Stowe MC, Cruz FC, Marian A, Ye J. 2006. High resolution atomic coherent control via spectral phase manipulation of an optical frequency comb. *Phys. Rev. Lett.* 96:153001
40. Stowe MC, Pe'er A, Ye J. 2008. Control of four-level quantum coherence via discrete spectral shaping of an optical frequency comb. *Phys. Rev. Lett.* 100:203001
41. Li C-H, Benedick AJ, Fendel P, Glenday AG, Kärtner FX, et al. 2008. A laser frequency comb that enables radial velocity measurements with a precision of 1 cm s^{-1}. *Nature* 452:610–12
42. Steinmetz T, Wilken T, Araujo-Hauck C, Holzwarth R, Hänsch TW, et al. 2008. Laser frequency combs for astronomical observations. *Science* 321:1335–37
43. Ye J. 2004. Absolute measurement of a long, arbitrary distance to less than an optical fringe. *Opt. Lett.* 29:1153–55
44. Balling P, Křen P, Mašika P, van den Berg SA. 2009. Femtosecond frequency comb based distance measurement in air. *Opt. Express* 17:9300–13
45. Coddington I, Swann WC, Nenadovic L, Newbury NR. 2009. Rapid and precise absolute distance measurements at long range. *Nat. Photonics* 3:351–56
46. Stowe MC, Thorpe MJ, Pe'er A, Ye J, Stalnaker JE, et al. 2008. Direct frequency comb spectroscopy. *Adv. Atom. Mol. Opt. Phys.* 55:1–60
47. Ni K-K, Ospelkaus S, de Miranda MHG, Pe'er A, Neyenhuis B, et al. 2008. A high-phase-space-density gas of polar molecules. *Science* 322:231–35
48. Danzl JG, Haller E, Gustavsson M, Mark MJ, Hart R, et al. 2008. Quantum gas of deeply bound ground state molecules. *Science* 321:1062–66
49. Eyler EE, Chieda DE, Stowe MC, Thorpe MJ, Schibli TR, Ye J. 2008. Prospects for precision measurements of atomic helium using direct frequency comb spectroscopy. *Eur. Phys. J. D* 48:43–55
50. Yost DC, Schibli TR, Ye J, Tate JL, Hostetter J, et al. 2009. Vacuum-ultraviolet frequency combs from below-threshold harmonics. *Nat. Phys.* 5:815–20
51. Fortier TM, Jones DJ, Ye J, Cundiff ST, Windeler RS. 2002. Long-term carrier-envelope phase coherence. *Opt. Lett.* 27:1436–38
52. McFerran JJ, Swann WC, Washburn BR, Newbury NR. 2006. Elimination of pump-induced frequency jitter on fiber-laser frequency combs. *Opt. Lett.* 31:1997–99
53. Schibli TR, Hartl I, Yost DC, Martin MJ, Marcinkevičius A, et al. 2008. Optical frequency comb with submillihertz linewidth and more than 10 W average power. *Nat. Photonics* 2:355–59
54. Kim Y, Kim S, Kim Y-J, Hussein H, Kim S-W. 2009. Er-doped fiber frequency comb with mHz relative linewidth. *Opt. Express* 17:11972–77
55. Russel PStJ. 2003. Photonic crystal fibers. *Science* 299:358–62
56. Knight JC. 2003. Photonic crystal fibres. *Nature* 424:847–51
57. Matos L, Kleppner D, Kuzucu O, Schibli TR, Kim J, et al. 2004. Direct frequency comb generation from an octave-spanning, prismless Ti:sapphire laser. *Opt. Lett.* 29:1683–85
58. Fortier TM, Bartels A, Diddams SA. 2006. Octave-spanning Ti:sapphire laser with a repetition rate >1 GHz for optical frequency measurements and comparisons. *Opt. Lett.* 31:1011–13
59. Bartels A, Heinecke D, Diddams SA. 2008. Passively mode-locked 10 GHz femtosecond Ti:sapphire laser. *Opt. Lett.* 33:1905–7
60. Rauschenberger J, Fortier TM, Jones DJ, Ye J, Cundiff ST. 2002. Control of the frequency comb from a modelocked erbium-doped fiber laser. *Opt. Express* 10:1404–10

61. Tauser F, Leitenstorfer A, Zinth W. 2003. Amplified femtosecond pulses from an Er:fiber system: nonlinear pulse shortening and self-referencing detection of the carrier-envelope phase evolution. *Opt. Express* 11:594–600
62. Washburn BR, Diddams SA, Newbury NR, Nicholson JW, Yan MF, Jørgensen CG. 2004. Phase-locked, erbium-fiber-laser-based frequency comb in the near infrared. *Opt. Lett.* 29:250–52
63. Schibli TR, Minoshima K, Hong F-L, Inaba H, Onae A, et al. 2004. Frequency metrology with a turnkey all-fiber system. *Opt. Lett.* 29:2467–69
64. Adler F, Moutzouris K, Leitenstorfer A, Schnatz H, Lipphardt B, et al. 2004. Phase-locked two-branch erbium-doped fiber laser system for long-term precision measurements of optical frequencies. *Opt. Express* 12:5872–80
65. Desurvire E, Bayart D, Desthieux B, Bigo S. 2002. *Erbium-Doped Fiber Amplifiers: Device and System Developments*. New York: Wiley
66. Okuno T, Onishi M, Kashiwada T, Ishikawa S, Nishimura M. 1999. Silica-based functional fibers with enhanced nonlinearity and their applications. *IEEE J. Sel. Top. Quantum Electron.* 5:1385–91
67. Hartl I, Schibli TR, Marcinkevičius A, Yost DC, Hudson DD, et al. 2007. Cavity-enhanced similariton Yb-fiber laser frequency comb: 3×10^{14} W/cm^2 peak intensity at 136 MHz. *Opt. Lett.* 32:2870–72
68. Hartl I, Ruehl A, Thapa R, McKay HA, Thomas BK, et al. 2009. *Rapidly scanning Fourier transform spectrometer based on a GHz repetition rate Yb-fiber laser pair*. Presented at Conf. Lasers Electro-Opt. (CLEO 2009), Baltimore
69. Yost DC, Schibli TR, Ye J. 2008. Efficient output coupling of intracavity high-harmonic generation. *Opt. Lett.* 33:1099–101
70. Bernhardt B, Ozawa A, Holzwarth R, Udem T, Pupeza I, et al. 2009. *Frequency comb generation in the XUV regime using a Yb-fiber laser and amplifier system*. Presented at Conf. Lasers Electro-Opt. (CLEO 2009), Baltimore
71. Adler F, Cossel KC, Thorpe MJ, Hartl I, Fermann ME, Ye J. 2009. Phase-stabilized, 1.5-W frequency comb at 2.8–4.8 μm. *Opt. Lett.* 34:1330–32
72. Rothman LS, Gordon IE, Barbe A, Chris Benner D, Bernath PF, et al. 2009. The HITRAN 2008 molecular spectroscopy database. *J. Quant. Spectrosc. Radiat. Transf.* 110:533–72
73. Wang CY, Kuznetsova L, Gkortsas VM, Diehl L, Kärtner FX, et al. 2009. Mode-locked pulses from mid-infrared quantum cascade lasers. *Opt. Express* 17:12929–43
74. Kaindl RA, Eickemeyer F, Woerner M, Elsaesser T. 1999. Broadband phase-matched difference frequency mixing of femtosecond pulses in GaSe: experiment and theory. *Appl. Phys. Lett.* 75:1060–62
75. Huber R, Brodschelm A, Tauser F, Leitenstorfer A. 2000. Generation and field-resolved detection of femtosecond electromagnetic pulses tunable up to 41 THz. *Appl. Phys. Lett.* 76:3191–93
76. Zimmermann M, Gohle C, Holzwarth R, Udem T, Hänsch TW. 2004. Optical clockwork with an offset-free difference-frequency comb: accuracy of sum- and difference-frequency generation. *Opt. Lett.* 29:310–12
77. Foreman SM, Marian A, Ye J, Petrukhin EA, Gubin MA, et al. 2005. Demonstration of a HeNe/CH_4-based optical molecular clock. *Opt. Lett.* 30:570–72
78. Shelton RK, Ma L-S, Kapteyn HC, Murnane MM, Hall JL, Ye J. 2001. Phase-coherent optical pulse synthesis from separate femtosecond lasers. *Science* 293:1286–89
79. Foreman SM, Jones DJ, Ye J. 2003. Flexible and rapidly configurable femtosecond pulse generation in the mid-IR. *Opt. Lett.* 28:370–72
80. Tauser F, Adler F, Leitenstorfer A. 2004. Widely tunable sub-30-fs pulses from a compact erbium-doped fiber source. *Opt. Lett.* 29:516–18
81. Erny C, Moutzouris K, Biegert J, Kühlke D, Adler F, et al. 2007. Mid-infrared difference-frequency generation of ultrashort pulses tunable between 3.2 and 4.8 μm from a compact fiber source. *Opt. Lett.* 32:1138–40
82. Gambetta A, Ramponi R, Marangoni M. 2008. Mid-infrared optical combs from a compact amplified Er-doped fiber oscillator. *Opt. Lett.* 33:2671–73
83. Adler F, Sell A, Sotier F, Huber R, Leitenstorfer A. 2007. Attosecond relative timing jitter and 13 fs pulses from a two-branch Er:fiber laser. *Opt. Lett.* 32:3504–6

84. Lopez-Alvarez P, Brown CTA, Reid DT, Sibbett W, Missey M. 1999. High-repetition-rate ultrashort-pulse optical parametric oscillator continuously tunable from 2.8 to 6.8 μm. *Opt. Lett.* 24:1523–25
85. Marzenell S, Beigang R, Wallenstein R. 1999. Synchronously pumped femtosecond optical parametric oscillator based on $AgGaSe_2$ tunable from 2 μm to 8 μm. *Appl. Phys. B* 69:423–28
86. Andres T, Haag P, Zelt S, Meyn J-P, Borsutzky A, et al. 2003. Synchronously pumped femtosecond optical parametric oscillator of congruent and stoichiometric MgO-doped periodically poled lithium niobate. *Appl. Phys. B* 76:241–44
87. Südmeyer T, Innerhofer E, Brunner F, Paschotta R, Usami T, et al. 2004. High-power femtosecond fiber-feedback optical parametric oscillator based on periodically poled stoichiometric $LiTaO_3$. *Opt. Lett.* 29:1111–13
88. Sun JH, Gale BJS, Reid DT. 2007. Composite frequency comb spanning 0.4–2.4 μm from a phase-controlled femtosecond Ti:sapphire laser and synchronously pumped optical parametric oscillator. *Opt. Lett.* 32:1414–16
89. Reid DT, Gale BJS, Sun J. 2008. Frequency comb generation and carrier-envelope phase control in femtosecond optical parametric oscillators. *Laser Phys.* 18:87–103
90. Gebs R, Dekorsy T, Diddams SA, Bartels A. 2008. 1-GHz repetition rate femtosecond OPO with stabilized offset between signal and idler frequency comb. *Opt. Express* 16:5397–405
91. Bhupathiraju KV, Seymour AD, Ganikhanov F. 2009. Femtosecond optical parametric oscillator based on periodically poled stoichiometric $LiTaO_3$ crystal. *Opt. Lett.* 34:2093–95
92. White JU. 1942. Long optical paths of large aperture. *J. Opt. Soc. Am.* 32:285–85
93. Herriott DR, Schulte HJ. 1965. Folded optical delay lines. *Appl. Opt.* 4:883–89
94. DeVoe RG, Fabre C, Jungmann K, Hofnagle J, Brewer RG. 1988. Precision optical-frequency-difference measurement. *Phys. Rev. A* 37:1802–5
95. Hood CJ, Kimble HJ, Ye J. 2001. Characterization of high-finesse mirrors: loss, phase shifts, and mode structure in an optical cavity. *Phys. Rev. A* 64:033804
96. Thorpe MJ, Jones RJ, Moll K, Ye J, Lalezari R. 2005. Precise measurements of optical cavity dispersion and mirror coating properties via femtosecond combs. *Opt. Express* 13:882–88
97. Schliesser A, Gohle C, Udem T, Hänsch TW. 2006. Complete characterization of a broadband high-finesse cavity using an optical frequency comb. *Opt. Express* 14:5975–83
98. Hammond TJ, Mills AK, Jones DJ. 2009. Simple method to determine dispersion of high-finesse optical cavities. *Opt. Express* 17:8998–9005
99. Johnston PS, Lehmann KK. 2008. Cavity enhanced absorption spectroscopy using a broadband prism cavity and a supercontinuum source. *Opt. Express* 16:15013–23
100. Lehmann KK, Johnston PS, Rabinowitz P. 2009. Brewster angle prism retroreflectors for cavity enhanced spectroscopy. *Appl. Opt.* 48:2966–78
101. Schwarzl T, Eibelhuber M, Heiss W, Kaufmann E, Springholz G, et al. 2007. Mid-infrared high finesse microcavities and vertical-cavity lasers based on IV-VI semiconductor/BaF_2 broadband Bragg mirrors. *J. Appl. Phys.* 101:093102
102. Jones RJ, Diels J-C. 2001. Stabilization of femtosecond lasers for optical frequency metrology and direct optical to radio frequency synthesis. *Phys. Rev. Lett.* 86:3288–91
103. Jones RJ, Thomann I, Ye J. 2004. Precision stabilization of femtosecond lasers to high-finesse optical cavities. *Phys. Rev. A* 69:051803R
104. Ye J, Ma L-S, Hall JL. 1998. Ultrasensitive detections in atomic and molecular physics: demonstration in molecular overtone spectroscopy. *J. Opt. Soc. Am. B* 15:6–15
105. Schiller S. 2002. Spectrometry with frequency combs. *Opt. Lett.* 27:766–68
106. Keilmann F, Gohle C, Holzwarth R. 2004. Time-domain mid-infrared frequency-comb spectrometer. *Opt. Lett.* 29:1542–44
107. Coddington I, Swann WC, Newbury NR. 2008. Coherent multiheterodyne spectroscopy using stabilized optical frequency combs. *Phys. Rev. Lett.* 100:013902
108. Bartels A, Cerna R, Kistner C, Thoma A, Hudert F, et al. 2007. Ultrafast time-domain spectroscopy based on high-speed asynchronous optical sampling. *Rev. Sci. Instrum.* 78:035107
109. Bernhardt B, Ozawa A, Jacquet P, Jacquey M, Kobayashi Y, et al. 2010. Cavity-enhanced dual-comb spectroscopy. *Nat. Photonics* 4:55–57

110. Shirasaki M. 1996. Large angular dispersion by a virtually imaged phase array and its application to a wavelength demultiplexer. *Opt. Lett.* 21:366–68
111. Wang SX, Xiao S, Weiner AM. 2005. Broadband, high spectral resolution 2-D wavelength-parallel polarimeter for dense WDM systems. *Opt. Express* 13:9374–80
112. Xiao S, Weiner AM, Lin C. 2004. A dispersion law for virtually imaged phased-array spectral dispersers based on paraxial wave theory. *IEEE J. Quantum Electron.* 40:420–26
113. Griffiths PR, de Haseth JA. 2007. *Fourier Transform Infrared Spectrometry*. Hoboken: Wiley
114. Tillman KA, Maier RRJ, Reid DT, McNaughten ED. 2005. Mid-infrared absorption spectroscopy of methane using a broadband femtosecond optical parametric oscillator based on aperiodically poled lithium niobate. *J. Opt. A: Pure Appl. Opt.* 7:S408–14
115. Mandon J, Guelachvili G, Picqué N, Druon F, Georges P. 2007. Femtosecond laser Fourier transform absorption spectroscopy. *Opt. Lett.* 32:1677–79
116. Mandon J, Guelachvili G, Picqué N. 2009. Fourier transform spectroscopy with a laser frequency comb. *Nat. Photonics* 3:99–102
117. Miekisch W, Schubert JK, Noeldge-Schomburg GFE. 2004. Diagnostic potential of breath analysis—focus on volatile organic compounds. *Clin. Chim. Acta* 347:25–39
118. Amann A, Smith D, eds. 2005. *Breath Analysis for Clinical Diagnosis and Therapeutic Monitoring*. Singapore: World Sci.
119. Risby TH, Solga SF. 2006. Current status of clinical breath analysis. *Appl. Phys. B* 85:421–26
120. Cao W, Yixiang D. 2007. Current status of methods and techniques for breath analysis. *Crit. Rev. Anal. Chem.* 37:3–13
121. Repine JE, Bast A, Lankhorst I. 1997. Oxidative stress in chronic obstructive pulmonary disesase. *Am. J. Respir. Crit. Care Med.* 156:341–57
122. Alving K, Weitzberg E, Lundberg JM. 1993. Increased amount of nitric oxide in exhaled air of asthmatics. *Eur. Respir. J.* 6:1368–70
123. Horvát I, Donnely LE, Kiss A, Kharitonov SA, Lim S, et al. 1998. Combined use of exhaled hydrogen peroxide and nitric oxide in monitoring asthma. *Am. J. Respir. Crit. Care Med.* 158:1042–46
124. Phillips M, Cataneo RN, Ditkoff BA, Fisher P, Greenberg J, et al. 2003. Volatile markers of breast cancer in the breath. *Breast J.* 9:184–91
125. Phillips M, Cataneo RN, Cummin ARC, Gagliardi AJ, Gleeson K, et al. 2003. Detection of lung cancer with volatile markers in the breath. *Chest* 123:2115–23
126. Belda-Iniesta C, de Castro Carpeño J, Carrasco JA, Moreno V, Casado Sáenz E, et al. 2007. New screening method for lung cancer by detecting volatile organic compounds in breath. *Clin. Transl. Oncol.* 9:364–68
127. Crosson ER, Ricci KN, Richman BA, Chilese FC, Owano TG, et al. 2002. Stable isotope ratios using cavity ring-down spectroscopy: determination of $^{13}C/^{12}C$ for carbon dioxide in human breath. *Anal. Chem.* 74:2003–7
128. Bartlome R, Sigrist MW. 2009. Laser-based human breath analysis: D/H isotope ratio increase following heavy water intake. *Opt. Lett.* 34:866–68
129. Morgan VI. 1985. An oxygen isotope–climate record from the Law Dome, Antarctica. *Clim. Change* 7:415–26
130. Mosely-Thompson E, Thompson LG, Lin PN. 2006. A multi-century ice-core perspective on 20th-century climate change with new contributions from high-Arctic and Greenland (PARCA) cores. *Ann. Glaciol.* 43:42–48
131. Kerstel ERT, Iannone RQ, Chenevier M, Kassi S, Jost H-J, Romanini D. 2006. A water isotope (^{2}H, ^{17}O, and ^{18}O) spectrometer based on optical feedback cavity-enhanced absorption for in situ airborne applications. *Appl. Phys. B* 85:397–406
132. Plummer LN, Busenber E, Bohlke JK, Nelms DL, Michel RL, Schlosser P. 2001. Groundwater residence times in Shenandoah National Park, Blue Ridge Mountains, Virginia, USA: a multi-tracer approach. *Chem. Geol.* 179:93–111
133. Feng J, Clement R, Raynor M. 2008. Characterization of high-purity arsine and gallium arsenide epilayers grown by MOCVD. *J. Cryst. Growth* 310:4780–85

134. Cossel KC, Adler F, Bertness KA, Thorpe MJ, Feng J, et al. 2010. Analysis of trace impurities in semiconductor gas vie cavity-enhanced direct frequency comb spectroscopy. *Appl. Phys. B.* In press
135. Scoles G, Bassi D, Buck U, Laine DC, eds. 1988. *Atomic and Molecular Beam Methods*, Vol. 1. Oxford: Oxford Univ. Press
136. Tejada G, Maté B, Fernández-Sánchez JM, Montero S. 1996. Temperature and density mapping of supersonic jet expansions using linear Raman spectroscopy. *Phys. Rev. Lett.* 76:34–37
137. Dupré P. 2001. Probing molecular species by cavity ringdown laser absorption spectroscopy, application to the spectroscopy and dynamics of jet-cooled NO_2. *C. R. Acad. Sci. Paris* 2:929–64
138. Scherer JJ, Paul JB, O'Keefe A, Saykally RJ. 1997. Cavity ringdown laser absorption spectroscopy: history, development, and application to pulsed molecular beams. *Chem. Rev.* 97:25–51
139. Herman M, Georges R, Hepp M, Hurtmans D. 2000. High resolution Fourier transform spectroscopy of jet-cooled molecules. *Int. Rev. Phys. Chem.* 19:277–325
140. Herman M, Didriche K, Hurtmans D, Kizil B, Macko P, et al. 2007. FANTASIO: a versatile experimental set-up to investigate jet-cooled molecules. *Mol. Phys.* 105:815–23
141. Bracewell RN. 2000. *Fourier Transform and Its Applications*. New York: McGraw-Hill. 3rd ed.
142. Hansen EW, Jablokow A. 1982. State variable representation of a class of linear shift-variant systems. *IEEE Trans. Acoust. Speech Signal Proc.* 30:874–80
143. Carr LD, DeMille D, Krems RV, Ye J. 2009. Cold and ultracold molecules: science, technology and applications. *New J. Phys.* 11:055049
144. Hudson ER, Ticknor C, Sawyer BC, Taatjes CA, Lewandowski HJ, et al. 2006. Production of cold formaldehyde molecules for study and control of chemical reaction dynamics with hydroxyl radicals. *Phys. Rev. A* 73:063404
145. Krems RV. 2008. Cold controlled chemistry. *Phys. Chem. Chem. Phys.* 10:4079–92
146. Ospelkaus S, Ni KK, Wang D, de Miranda MHG, Neyenhuis B, et al. 2010. Quantum-state controlled chemical reactions of ultracold KRb molecules. *Science* 327:853–57

Annual Review of
Analytical Chemistry

Volume 3, 2010

Contents

Indexes

Errata

An online log of corrections to *Annual Review of Analytical Chemistry* articles may be found at http://arjournals.annualreviews.org/errata/anchem.